AFRL-RY-WP-TR-2020-0221

ULTRA-COMPACT RECONFIGURABLE INTEGRATED PHOTONIC PHASE SHIFTERS

Ali Adibi
Georgia Institute of Technology

AUGUST 2020
Final Report

STINFO COPY

AIR FORCE RESEARCH LABORATORY
SENSORS DIRECTORATE
WRIGHT-PATTERSON AIR FORCE BASE, OH 45433-7320
AIR FORCE MATERIEL COMMAND
UNITED STATES AIR FORCE

NOTICE AND SIGNATURE PAGE

Using Government drawings, specifications, or other data included in this document for any purpose other than Government procurement does not in any way obligate the U.S. Government. The fact that the Government formulated or supplied the drawings, specifications, or other data does not license the holder or any other person or corporation; or convey any rights or permission to manufacture, use, or sell any patented invention that may relate to them.

This report is the result of contracted fundamental research deemed exempt from public affairs security and policy review in accordance with The Under Secretary of Defense memorandum dated 24 May 2010 and AFRL/DSO policy clarification email dated 13 January 2020. This report is available to the general public, including foreign nationals.

Copies may be obtained from the Defense Technical Information Center (DTIC) (http://www.dtic.mil).

AFRL-RY-WP-TR-2020-0221 HAS BEEN REVIEWED AND IS APPROVED FOR PUBLICATION IN ACCORDANCE WITH ASSIGNED DISTRIBUTION STATEMENT.

*//Signature//

NICHOLAS G. USECHAK
Program Manager
Highly Integrated Microsystems Branch
Aerospace Components & Subsytems Division

*//Signature//

ATTILA A. SZEP, Chief
Highly Integrated Microsystems Branc
Aerospace Components & Subsytems Division

//Signature//

ADAM L. BROOKS, Lt Col, USAF
Deputy
Aerospace Components & Subsytems Division
Sensors Directorate

This report is published in the interest of scientific and technical information exchange, and its publication does not constitute the Government's approval or disapproval of its ideas or findings.

*Disseminated copies will show "//Signature//" stamped or typed above the signature blocks.

REPORT DOCUMENTATION PAGE

Form Approved
OMB No. 0704-0188

1. REPORT DATE *(DD-MM-YY)*	2. REPORT TYPE	3. DATES COVERED *(From - To)*
August 2020	Final	23 February 2018 – 23 February 2020

4. TITLE AND SUBTITLE
ULTRA-COMPACT RECONFIGURABLE INTEGRATED PHOTONIC PHASE SHIFTERS

5a. CONTRACT NUMBER
FA8650-18-1-7829

5b. GRANT NUMBER

5c. PROGRAM ELEMENT NUMBER
62716E

6. AUTHOR(S)
Ali Adibi

5d. PROJECT NUMBER
N/A

5e. TASK NUMBER
N/A

5f. WORK UNIT NUMBER
Y1RU

7. PERFORMING ORGANIZATION NAME(S) AND ADDRESS(ES)

Georgia Institute of Technology
777 Atlantic Drive NW
Atlanta, GA 30332-0250

8. PERFORMING ORGANIZATION REPORT NUMBER

9. SPONSORING/MONITORING AGENCY NAME(S) AND ADDRESS(ES)

Air Force Research Laboratory
Sensors Directorate
Wright-Patterson Air Force Base, OH 45433-7320
Air Force Materiel Command
United States Air Force

Defense Advanced Projects Agency
DARPA/MTO
675 North Randolph Street
Arlington, VA 22203

10. SPONSORING/MONITORING AGENCY ACRONYM(S)
AFRL/RYDI

11. SPONSORING/MONITORING AGENCY REPORT NUMBER(S)
AFRL-RY-WP-TR-2020-0221

12. DISTRIBUTION/AVAILABILITY STATEMENT
Approved for public release; distribution is unlimited.

13. SUPPLEMENTARY NOTES
This report is the result of contracted fundamental research deemed exempt from public affairs security and policy review in accordance with The Under Secretary of Defense memorandum dated 24 May 2010 and AFRL/DSO policy clarification email dated 13 January 2020. This material is based on research sponsored by the Air Force Research Lab (AFRL) and the Defense Advanced Research Agency (DARPA) under agreement number FA8650-18-2-7833. The U.S. Government is authorized to reproduce and distribute reprints for Governmental purposes not withstanding any copyright notation thereon. The views and conclusions contained herein are those of the authors and should not be interpreted as necessarily representing the official policies or endorsements, either expressed or implied, of AFRL and DARPA or the U.S. Government. Report contains color.

14. ABSTRACT
In this two-year seedling project Georgia Institute of Technology successfully demonstrated the unique features of the phase-change materials (PCMs) for enabling a new paradigm in design and implementation of reconfigurable integrated nano-photonic structures with unprecedented features. Although the overarching goal of this project was the demonstration of the ultra-miniaturized phase shifters for the Modular Optical Aperture Building Blocks (MOABB) program, the research has applicability well beyond the phase shifters originally focused on and enables the creation of a new platform that can be used to manipulate light strongly using subwavelength features. We strongly believe that the demonstrated hybrid Si (SiN)/PCM platform can address multiple challenges in the use of integrated photonics for state-of-the-art applications.

15. SUBJECT TERMS
integrated photonics, phase shifters, phase-change materials

16. SECURITY CLASSIFICATION OF:			17. LIMITATION OF ABSTRACT:	18. NUMBER OF PAGES	19a. NAME OF RESPONSIBLE PERSON (Monitor)
a. REPORT	b. ABSTRACT	c. THIS PAGE			Nicholas Usechak
Unclassified	Unclassified	Unclassified	SAR	45	19b. TELEPHONE NUMBER *(Include Area Code)* (937) 713-8851

Table of Contents

Section **Page**

List of Figures

Figure **Page**

Figure **Page**

Figure **Page**

List of Tables

Table **Page**

1 INTRODUCTION

This report summarizes the achievements of Dr. Adibi's research group at Georgia Institute of Technology (GTRI) under grant number FA8650-18-1-7829, which was an effort funded through Defense Advanced Research Projects Agency (DARPA) Modular Optical Aperture Building Blocks (MOABB) program. This report highlights the major achievements from February 15, 2018 until February 14, 2020 with brief descriptions. Additional information also can be found in the recent publications of our group or by reaching out to Dr. Adibi directly. The goal of this project was to develop an ultra-compact, low-power integrated photonic phase shifter with unprecedented performance for radio-frequency (RF) photonics, light detection and ranging (LiDAR), and free-space optical communications (FSOC) applications. The proposed solution is based on complementary metal–oxide–semiconductor (CMOS)-compatible materials (especially silicon (Si) and silicon nitride (SiN)) with phase-change materials (PCMs) that provide unprecedented change in their index of refraction upon conversion between amorphous and crystalline phases. The resulting hybrid integrated photonic platform enables photonic structures which are rapidly reconfigurable [within ~100 nanoseconds (ns)], have a low reconfiguration energy (consuming < 100 picoJoules (pJ) for a complete 2π optical phase change], and ultra-compact footprints (with subwavelength spatial dimensions). While the level of index change in PCMs can reduce the reconfigurable/tunable devices by 3-4 orders of magnitude compared to state-of-the-art Si photonic technologies, the non-volatility of devices based on phase changes enables a considerable reduction in power consumption under continuous operation. The use of PCMs also enables a myriad of thermal, optical, and electronic means of reconfiguration and can enable novel device architectures for a large range of applications. Nevertheless, the focus of this two-year project has been the design and demonstration of integrated photonic phase shifters with full electrical reconfiguration.

Through extensive theoretical and experimental efforts, this effort resolved all the fundamental challenges associated with the design, material processing, and fabrication of the proposed integrated phase-change based photonic phase shifters on the proposed hybrid platform. In contrast to the prior state-of-the-art in this area, which focused on optically actuating PCMs using ultra-short and energetic pulses, this effort was able to demonstrate, for the first time, a reliable material and device platform that enabled the electrical actuation of these PCMs on integrated photonic chips using indium tin oxide (ITO) heaters. This effort was also the first to demonstrate a complete multi-step phase change in germanium antimony telluride (GST). In this work, potentially as many as 100 intermediate crystalline phases were demonstrated enabling an analog-like operation of these phase shifters. Importantly, this was demonstrated along with a full re-amorphization and recycling of the multi-state conversion using electrical signals alone identifying that these devices can be set as well as "flashed" and re-used. The culmination of our efforts resulted in the first reported integrated photonic phase shifter technology with a reduction in size of more than 3 orders of magnitude, when compared to all existing alternatives. This device also has the potential for its footprint to be further reduced to having an overall size that is sub-wavelength. Although the optical insertion loss of these devices is still high, there is the possibility to address this by working with other PCMs. In general this technology should enable a new paradigm in forming miniaturized reconfigurable integrated photonic devices and systems over a wide wavelength range (visible to deep-infrared (IR)), which are urgently needed for a large range of DoD applications including LiDAR, optical signal processing, RF photonics,

imaging, and computing, as well as quantum information processing, communications, and sensing. As such, the results of this project should open a new avenue for research and development in the field with significant potential to address some of the long-lasting challenges associated with creating reconfigurable photonic and quantum devices and systems. Some potential areas where this technology could prove instrumental are discussed at the end of this report.

In the first phase of the program, we primarily focused on the fundamental infrastructure for the proposed platform and developed a complete understanding of what was needed to design hybrid PCM-based integrated photonic devices by considering all the electrical, optical, and thermal properties. This work included the performance of:

- the sputtering system — used to integrate the GST with CMOS-compatible materials (especially Si and SiN)
- a detailed fabrication process — for forming reconfigurable integrated photonic devices and systems in the GST-based hybrid platform,
- a detailed investigation of the thermal, optical, and electrical conversion techniques — to capture and understand GST's repeatable intermediate phase change, and an initial design of integrated photonic phase shifters in the hybrid platform.

Using these major achievements in the first year of this effort, we focused on the realization of miniaturized integrated photonic devices in the hybrid platform with many GST intermediate states during the second year. We studied all three approaches (i.e., thermal, optical, and electrical) for the GST crystalline phase change, and, through detailed optimization, were able to demonstrate the first electrically converted miniaturized phase shifter by the end of the second year. In this endeavor, we even surpassed some of our aggressive initial milestones. For example, by achieving multi-state GST phase conversion with full repeatability and as many as 100 states instead of our original target of 16 states we exceeded what we had thought could be demonstrated under this effort. Throughout these two years, we gained additional insight into the material and device architecture. As a result, the platform developed under this research is thoroughly unique and now has the potential to be adopted to address new applications in the visible and IR region as listed above. By addressing some of the remaining challenges in a follow-on program, we hope to extend this platform such that it is suitable for integrated nanophotonics in the entire visible-IR range, which could prove important for supporting applications in biology and atomic physics.

2 RESEARCH ACCOMPLISHMENTS

2.1 Analysis and Design of Integrated Photonic Phase Shifters based GST-Si and GST-SiN Platforms

2.1.1 Optical Design and Analysis

Phase shifters are of great interests for a wide range of applications including beam forming, routing, and LiDAR, to name a few. The physical mechanism used to realize a voltage-adjustable phase shift in Si photonics is typically based on a thermo-optic or plasma-dispersion effect, which provides only a small refractive index contrast. Accordingly, integrated photonic devices that rely on this mechanism suffer from large footprints and significant energy consumption is required to obtain useful phase shifts. To address these issues, we demonstrate the use of a hybrid Si/PCM platform enabling miniaturized and high-resolution phase shifters covering a 2π phase shift thanks to the unique optical properties of PCMs with large complex refractive index contrast between its different material states (from amorphous all the way to the crystalline with potentially continuous intermediate states). The realized devices afford zero static power consumption in their operational mode, owing to the non-volatility of PCMs, and the material state transition only requires a low-power short pulse excitation.

Considering the hybrid structure of our Si-PCM, there are different configurations that can be selected to implement a phase shifter. The most straightforward solution is to deposit PCM on top of a silicon waveguide and change the state of PCM to induce phase shift via the evanescent field propagating in the silicon. However, this only induces small phase shifts and our work sought to maximize the phase shift so we explored other configurations that would provide larger phase shifts on the side of a silicon waveguide. In this case, the field is switched between the Si and GST-PCM materials, because the amorphous state has smaller refractive index compared to Si, while the crystalline state has higher refractive index. This significant change in the mode profile hinders the efficient implementation of Si-GST along a silicon waveguide (the insertion loss of this design would be significant). This configuration is well suited for thin-GST to avoid significant change in the field profile at the cost of dimensions and propagation-loss. The latter is due to the high extinction coefficient of GST in its crystalline state, and in general for PCMs, where the higher refractive index is accompanied with a larger extinction coefficient.

Obtaining a large extinction coefficient between the amorphous and crystalline states is indeed a big hurdle for the use of PCMs in hybrid structures, which needs to be addressed by both material optimization and design concepts to mitigate situations in which the phase of the entire material does not change. There have been reports on the low loss GST-PCMs, yet it is noteworthy to mention that the reported refractive indices for GST-PCMs differ in the literature, which may be due different deposition processes and material stoichiometry. This issue is beyond the scope of this work, in which we focus on harnessing design features combined with the best material parameters reported in literature to implement a high-resolution, low-power, miniaturized phase shifter based on a hybrid Si-GST platform. The reported complex refractive indices for GST-225 are: $\mathrm{n_a} = 2.42 - i0.05$, and $\mathrm{n_c} = 5.25 - 0.1$ [APL, 109(5), 051103], for operation at 1550 nm. We use these parameters for our designs.

To achieve miniaturized, high-resolution phase shifters, we need to implement the reconfigurable element along the waveguide co-directionally and avoid coupling to any element causing an on-resonant/off-resonant phase shift. In such a configuration, the incoming wave is divided between two sections, and the relative phase in-between would show itself at the output, at the expense of relatively large losses. Thus, it is necessary to implement the desired structure in form of an in-plane phase shift. Although the former suffers from a vector-sum mismatch, it relaxes criteria on the field profile in each segment. The latter topology, i.e. an in-plane phase shifter, address the concerns related to vector summation, it includes a field discontinuity at the interface between the silicon waveguide and the phase shift element. This would further complicate the structure due to the limited number of available stable intermediate states in GST-PCM which can be achieved via the control signal. To address these issues multiple sections would be required to achieve the desired high resolution.

Furthermore, to mitigate the material loss in the crystalline state, we leverage the higher refractive index of GST at its crystalline state in a GST-Si-GST configuration. This configuration forms a slot waveguide, where most of the electric field is confined in the low-loss silicon region, while in the amorphous state, the field extends well into the surrounding GST, as it has lower refractive index. This enables us to combine the advantageous large refractive index change in GST with its high extinction coefficient by forming a slot waveguide. This topology forces the light to be confined in the silicon waveguide rather than in the GST-crystalline. Figure 1 demonstrates this structure in which the Si waveguide is etched and back filled with GST to make a more robust phase shifter. The electric-field distribution of the fundamental quasi-TE mode is also shown, highlighting the mode-change in-between the two states of GST.

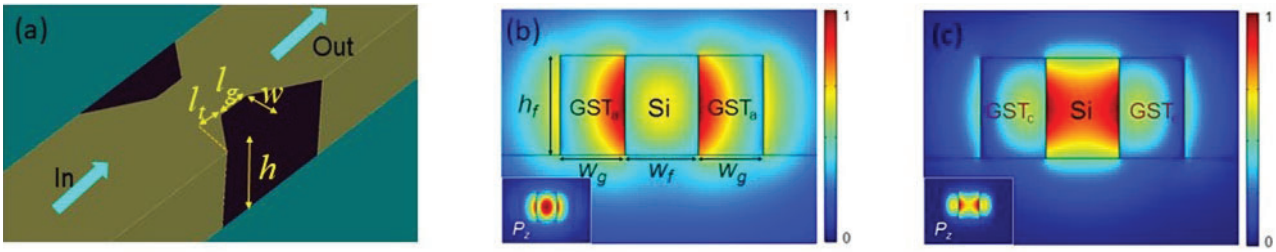

Figure 1: Hybrid Waveguide Phase Shifter

a) Schematic of the in-plane phase shifter using GST-Si-GST along the Si waveguide. The phase shifter is also tapered to reduce the field profile mismatch between the silicon waveguide and the GST-Si-GST "active" segment. The electric-field profile of the fundamental quasi-TE mode is shown for the GST-amorphous and crystalline states in (b) and (c), respectively. The inset in these two figures represents the pointing vector along the propagation direction.

As mentioned before, for a discrete number of total available states in the PCM, we need to cascade multiple of phase shifters to increase the total space spanned by more than one phase shifter. For design purposes, we focus on the 16 states of GST that have been studied in literature. In order to provide a systematic approach, we first design a phase shifter which divides a 2π phase shift into 16 steps, each addressable with appropriate signaling of the first phase shifter. Thus, the first phase shifter would provide a coarse phase shift over a wide range. Then, the second phase shifter would provide a higher-resolution phase shift but over a much smaller range. Extending this approach it is possible to achieve a high-resolution phase shifter.

Figure 2 represents a two-segment phase shifter implemented using the platform described above, where the first phase shifter provides a coarse-resolution phase shift while the second one provides a high-resolution phase shift.

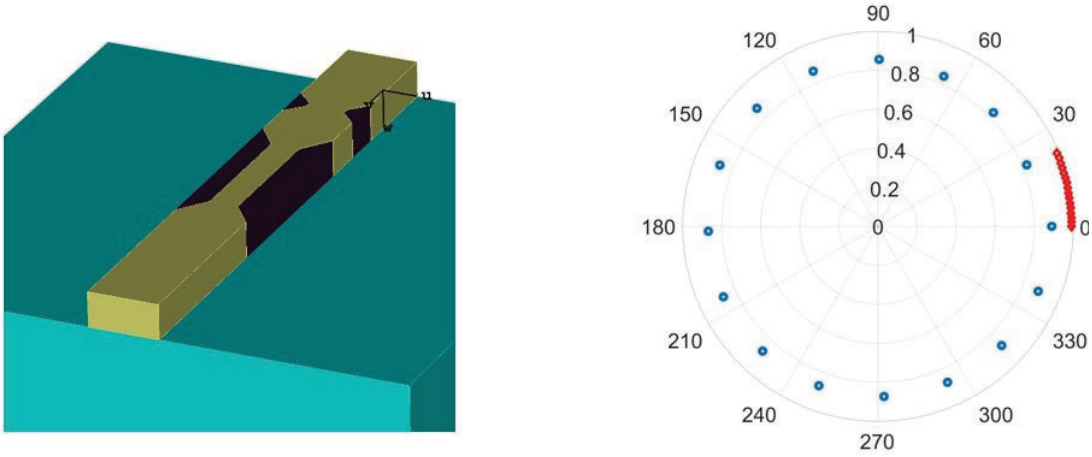

Figure 2: Schematic of the Two-section Phase Shifter

The first phase shifter provides coarse phase shifts, covering the entire 2π space when switched between amorphous and crystalline states. The smaller phase shifter is designed to cover $\frac{2\pi}{16}$ in 16 steps.

To study the total space covered by the two phase shifters, we adjust and optimize the spacing between them, and also their geometrical configurations to minimize any Fabry–Perot effects which can otherwise change the overall phase and add (wavelength dependent) loss. Figure 3 demonstrates the total space covered by 16^2 states of two GST-Si-GST phase shifters.

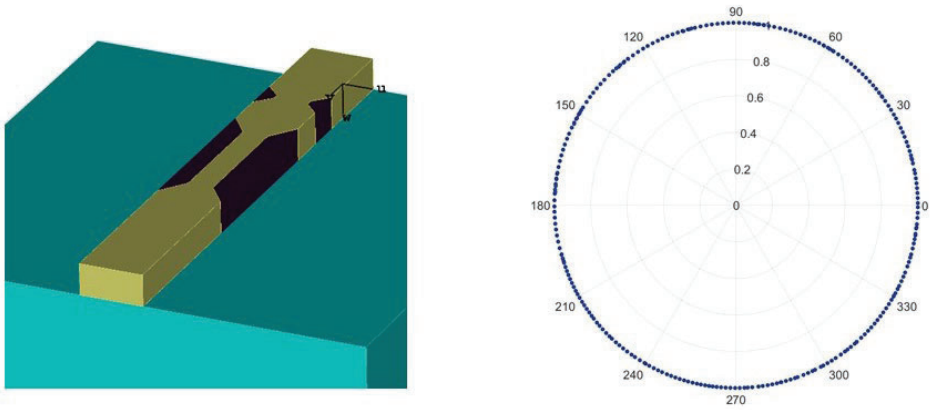

Figure 3: Schematic and Simulation Results for a Two-stage Phase Shifter

With coarse and fine phase shift segments, each made up of GST-Si-GST along the Si waveguide, on oxide and air clad. The simulation results for 256 states of the combined space of phase shifters. The maximum angular distance is 2 degrees and the loss, excluding material loss is below 0.1 decibel (dB).

One important feature of the phase shifter is relative loss through the dynamic tuning of the structure. To study this we consider the material loss, with the parameters mentioned before for the best material characteristics of GST. Figure 4 represents and loss variation through the 256 states of the phase shifter. As shown, the relative loss is less than 0.7 dB across the entire 2π phase tuning range, while the phase-shift resolution is better than 2.2 degrees.

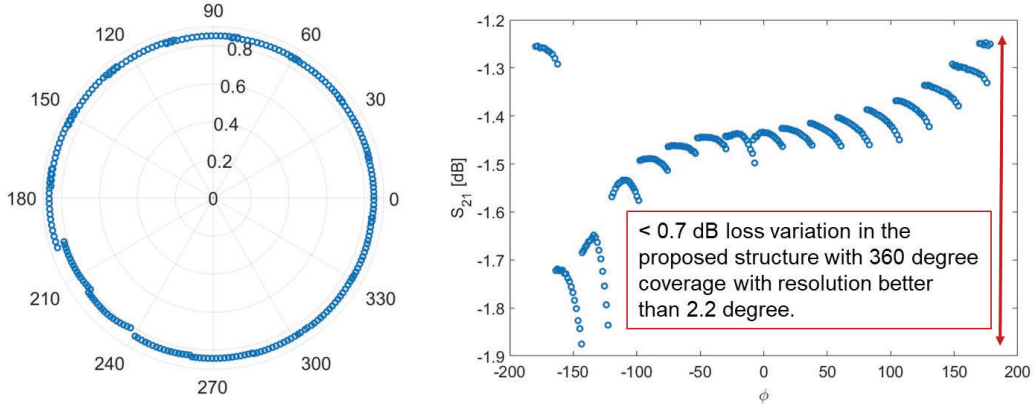

Figure 4: Polar Plot of the Two-stage Phase Shifter with the same Parameters as used in Figure 2, except Material Loss has now also been included in these Simulations
The scattering parameter s_{21} is also shown to study the dynamic range of the transmitted amplitude, which shows a relative loss of less than 0.7 decibels (dB).

Therefore, the two-stage phase shifter implemented in our silicon photonics platform was created with an optimized design using the best material parameters reported in literature. It should be noted that it is still a major challenge to realize this level of performance in practice and it has not been reported elsewhere. Nonetheless, we presented a path forward using mode engineering to leverage the change in modes and to mitigate the losses associated with the crystalline state of the GST-PCM. This is achieved in the GST-Si-GST platform, when the refractive indices of the GST-PCM is changed to switch the mode profile from a standard-looking waveguide mode to one that looks like one that is localized in the slot waveguide. The majority of the field resides in the GST in normal operation mode, while it is localized in the narrow silicon waveguide, thus managing the propagation loss.

2.1.2 Thermal Crosstalk Mitigation

Minimizing the thermal crosstalk between neighboring GST segments is a critical design consideration for the successful operation of the phase shifter configuration discussed above. Indeed, it is essential to be able to change the crystalline phase of only the intended GST segment while not affecting others. In searching for an ideal geometrical condition that secures the minimum thermal crosstalk, we solve the three dimensional (3D) time-transient heat-transfer equation ($C_s\rho\partial T/\partial t + \nabla.(-k\nabla T) = Q_s$) using COMSOL Multiphysics. Here, T, t, k, C_s, and ρ are temperature, time, thermal conductivity, heat capacitance at constant pressure, and mass volume, respectively. The quantitative values used in our simulations are tabulated in Table 1(a). In this table, the electrical conductance of the GST is treated as a semiconductor with a temperature dependent electrical conductivity of $\sigma = \sigma_0 \exp(-E_a/k_bT)$ with $\sigma_0 = 1.7\times 10^6$ $(\Omega\text{-m})^{-1}$ and $E_a = 0.14$ eV where E_a is the thermal activation energy (Note: these values were taken from

the literature). The thermal conductivity of GST was also considered temperature dependent and modeled using values from the literature (see: Microelectronic Engineering 84 (2007) 1792–1796).

Without losing generality, we consider Joule heating as the heat source (i.e., Q_s) in the heat-transfer equation. Thus, considering a current density of J, the heat source can be calculated as $Q_s = J^2/\sigma$, where σ is the material's electrical conductivity. In addition, at all interfaces, we also consider uniform thermal boundary-resistance (TBR) values defined as $R_{TBR} = \Delta T/Q_s$. The quantitative values of R_{TBR}s used in our simulations are tabulated in Table 1(b). It is worth noting that other types of thermal stimuli used for GST conversion, can be modeled by changing the heat source from Joule heating to e.g. optical absorption (for laser-induced heating of GST).

Table 1. Material Parameters used in our 3D Time-transient Heat-transfer Equation

(See Microelectronic Engineering 84 (2007) 1792–1796)

(a)

	C_s (J/(Kg.K))	ρ (Kg/m^3)	k (W/(m.K))	σ (S/m)
GST	220	6150	T dependent [1]	T dependent (above)
SiO_2	741	2200	1	0
Air	1	353/T[K]	0.03	0
Si	700	2328	130	1000

(b)

	GST/SiO_2	GST/Au	otherwise
R_{TBR} (m^2. K)/GW	58	5.1	25

To optimize our device geometry for minimizing thermal crosstalk, we consider the phase shifter with multiple GST segments as shown in Figure 5(a). Considering the worst-case scenario, we assume that the largest GST segment is excited with an electrical pulse of a given width, and then we trace the temporal evolution of the temperature across the entire phase shifter, especially in the GST segment closest to the excited segment. The minimum thermal crosstalk is achieved when the heat profile is confined in the excited segment with minimum extension into the neighboring segment. Figure 5(b) represents the sequence of temperature profiles (at different times relative to the exiting pulse) for an optimized geometry in which GST segments are placed 200 nm apart. In this example, the largest GST segment is excited with a 100-ns wide electric pulse. The pulse amplitude is tuned to ensure temperature reaches ~ 800 K at which fast amorphous-to-crystalline conversion is expected. As shown in Figure 5(b), the generated heat is initially confined in the excited segment and builds up from room temperature to 600 K in ~50 nsec; the temperature continues to increase and reaches 800 K around 200 nsec. Later, an observable diffusion of heat into the neighboring GST segment emerges. However, the maximum temperature in the neighboring segment never exceeds 400 K (i.e., 100ºC), a temperature at which the kinetics of phase change in GST is extremely slow, and virtually nonexistent within the width of the excitation pulse. We would like to emphasis that the speed of the crystalline phase change exponentially varies with temperature. So, a momentary temperature increase in the neighboring GST section (e.g., ~ 420 K) cannot drive a significant phase change during a short excitation pulse that is applied to another GST section. Thus, the 200-nm separation between GST sections is enough to provide effective thermal isolation for the phase shifters.

To emphasis the importance of short electrical pulses for minimizing the thermal crosstalk, we changed the pulse width and monitored the temperature evolution in the GST segment adjacent to the excited segment. As shown in Figure 5(c), by increasing the pulse width from 100 ns to 500 ns and then to1000 ns, the maximum temperature in the neighboring GST segment increases from ~ 420 K to ~ 470 K and then to ~ 500 K, respectively. This identifies that that the phase conversion in the GST using a short electrical pulse can significantly mitigate the thermal crosstalk between GST pairs in our proposed phase shifter structure.

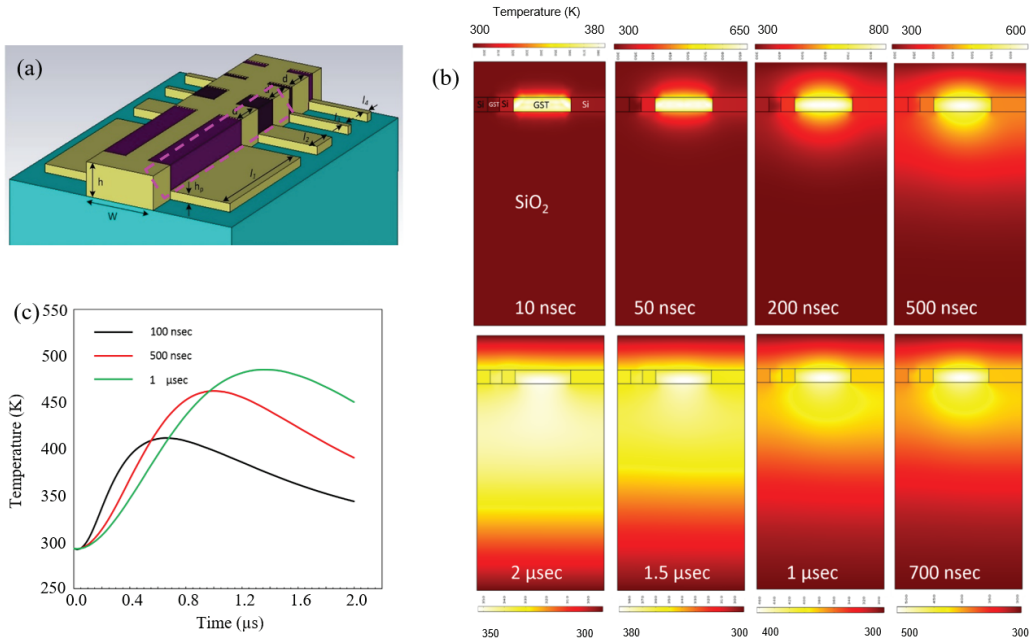

Figure 5: Mitigation of Thermal Crosstalk in Multi-segment GST/Si Phase Shifter
(a) Schematic of the simulated structure. Yellow, purple, and cyan represent Si, GST, and SiO_2, respectively. (b) Temporal evolution of the temperature profile across the highlighted region in panel (a), under a 100-ns wide electrical pulse applied to the largest GST segment. (c) The maximum temperature obtained in the neighboring GST segment (i.e., the smaller of the two GSTs shown in dashed box in (a)), under various pulse width applied to the large GST segment.

2.2 Development of a Complete Material Preparation and Fabrication Approach for GST

To support the fabrication of GST-based phased shifters this work required that we develop a custom sputtering system. The home-built RF sputtering system consisted of a main chamber with three perpendicular guns where GST, germanium telluride (GeTe), and ITO targets are installed and a load-lock chamber, with the capacity of one four-inch wafer to isolate the direct exposure to the main chamber and to increase safety levels, prevent target oxidation, and minimize chamber contamination. The system was controlled through custom home-made software to facilitate its operation. The final system allows the user to co-sputter two materials. The capability to in-situ deposit ITO guarantees oxidation prevention of the deposited PCM after being exposed to the ambient environment. Figure 6 represent the overall system configuration with the main parts included as insets.

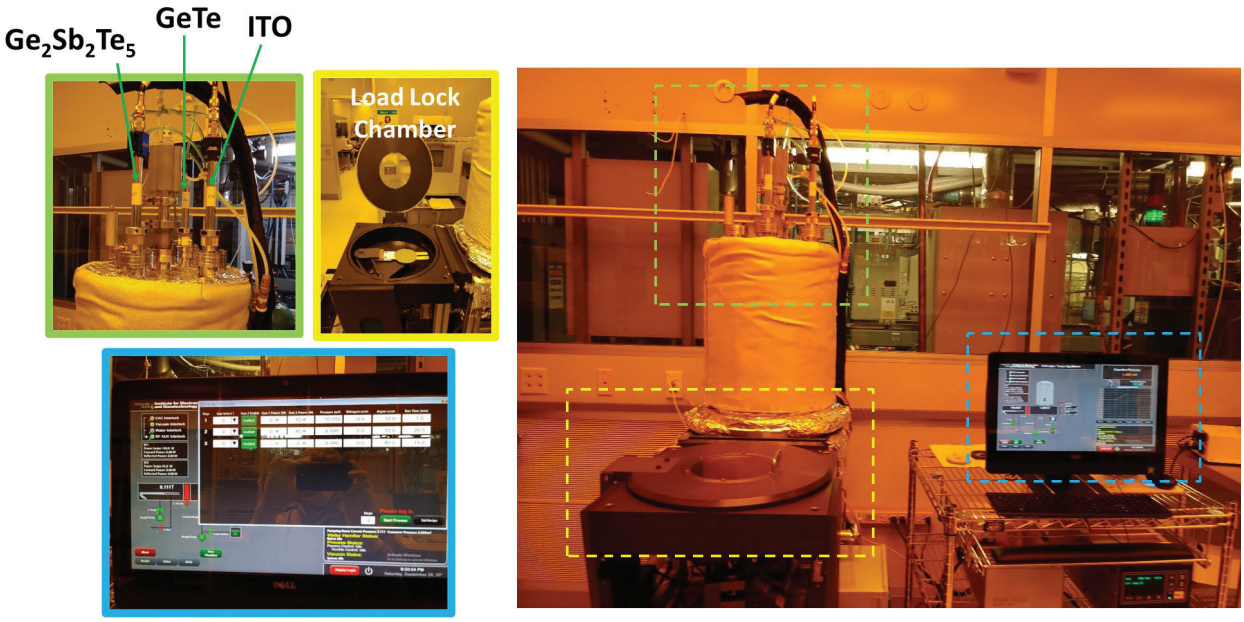

Figure 6: Home-built Sputtering System Facilitating Co-deposition of PCMs (GST and GeTe) and In-situ Deposition of ITO as the Capping Layer to Hamper Oxidation of Ambient-exposed Sample

The main parts of the system are enlarged in the insets.

To determine the binding energies of the core electrons in the amorphous GST (a-GST) films, X-ray photoelectron spectroscopy (XPS) was performed. To remove surface contamination as well as oxidation, samples were sputtered with Ar ions with an energy of 0.5 KeV and a current density of approximately10 uA/cm^2 resulting in a spot size of tens of micrometers. This leads to an improvement in the intensity peak found in the survey scan of the alloy. We carried out the survey scan within the binding energy range of 0-600 eV and the core-level spectra of elements is plotted in Figure 7.

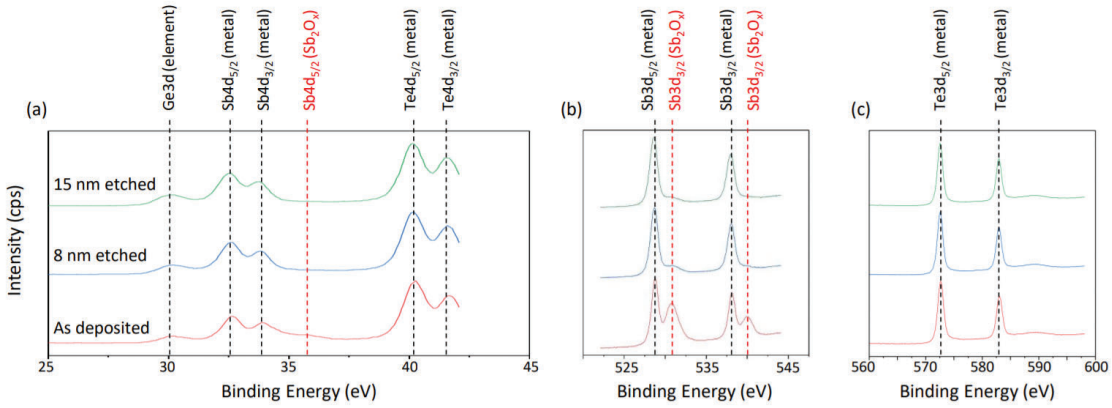

Figure 7: Surface Oxidation of Unprotected GST under Ambient Conditions
(a) XPS spectra of Ge 3d, Sb 4d, and Te 4d levels obtained from the surface, 8 nm below the surface, and 15 nm below the surface of a GST film without the capping layer. (b, c) XPS spectra of Sb 3d, and Te 3d, respectively. The oxidation is primarily reflected in the Sb photoemission lines obtained from the topmost GST surface. The thickness of the as-deposited GST layer was 50 nm.

In this work we used an inVia Qontor confocal Raman microscope (with a 100X objective) to study the Raman scattering in a micro-Raman configuration from a thin film of GST in as-deposited, crystalline, and re-amorphous states illuminated by the primary 785-nm laser. The power and integration time were set to 0.3 milliwatt (mW) and 10 s, respectively, in all cases to prevent crystallization and possible ablation during our measurements. Figure 8 clearly shows that the as-deposited and amorphous states poses a rather broad peak which converts to a dual-band peak upon transition to the crystalline phase. The broad peak in the amorphous state is due to vibrations of defective octahedra formed by Te, Sb, and a majority of the Ge atoms while the induced dual peaks in the crystalline state corresponds to the larger spread in the Ge-Te and Sb-Te bond lengths.

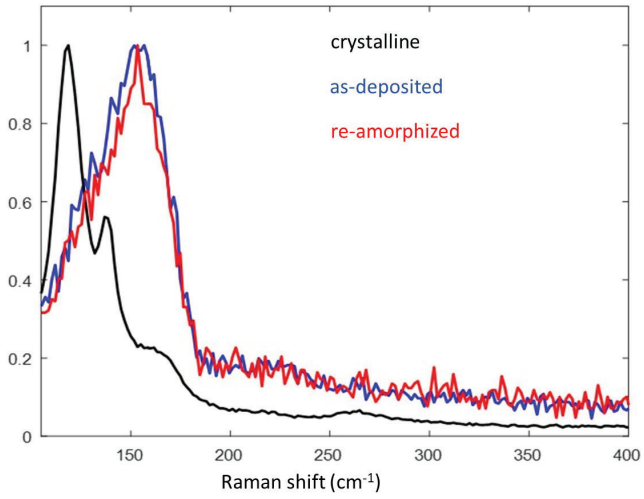

Figure 8: Raman Spectra of Crystalline and Amorphous GST Films
Crystallization was induced following laser exposure (785 nm, 0.3 mW, 10 s).

The complex refractive index of GST thin films was determined using a Woollam M-2000 Ellipsometer. The spectroscopic ellipsometery measurements were performed at three angles of incidence (50°, 60°, 70°) over spectral ranges from 1000 to 2000 nm (see Figure 9). Oscillator parameters as well as the thicknesses of the GST film and its surface roughness were used as fitting parameters. Tauc–Lorentz and Cody–Lorentz models were employed for the evaluation of optical functions of thin films in as-deposited and crystalline states. The model's parameters including Lorentz oscillator amplitude, resonance energy, oscillator width, optical band gap, and Urbach energy were chosen as fitting parameters.

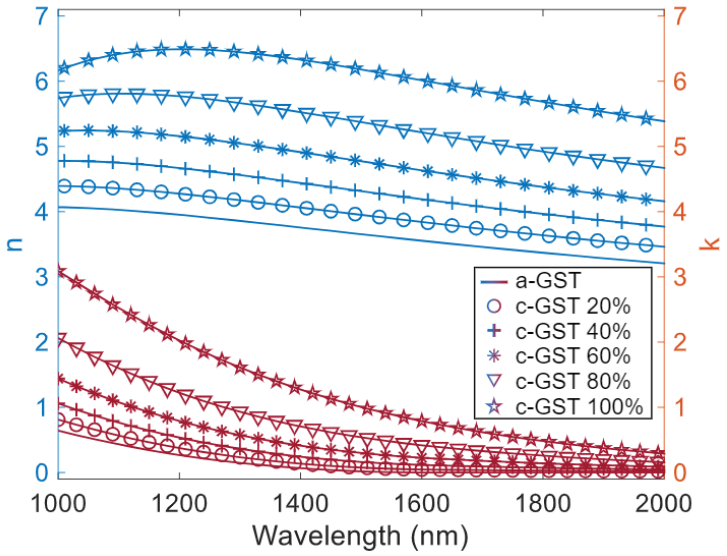

Figure 9: Evolution of the Real (n) and Imaginary (k) Part of the GST Refractive Index from Amorphous to Crystalline State

The topography of the as-deposited and crystalline thin films of GST were studied using atomic-force microscopy (AFM), as shown in Figure 10. The results are in good agreement with laser-crystallization results for the same film. The rather rough surface found in the crystalline state is the main source of optical scattering.

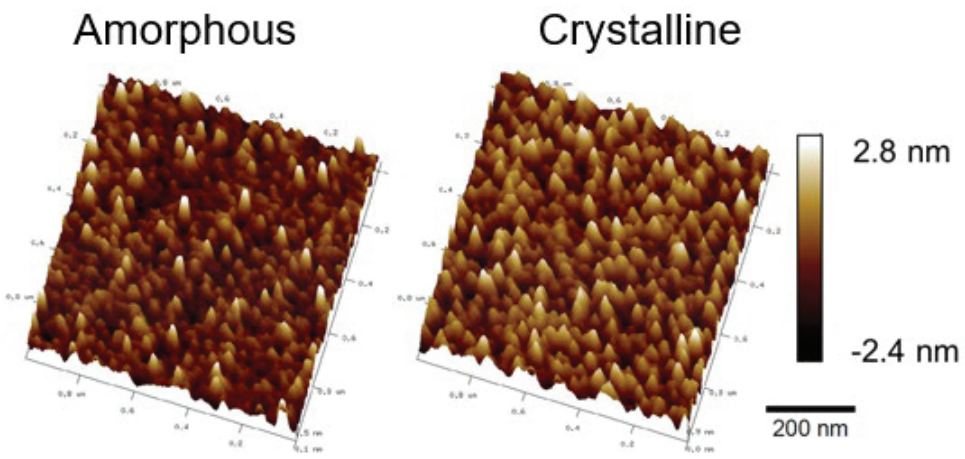

Figure 10: AFM imaging of the GST Films in Amorphous (left) and Crystalline (right) States

Film compaction occurs following the crystallization of the amorphous film.

The cross-sectional view of the as-deposited and crystalline GST film are shown in Figure 11. It is notable that the thermally induced crystalline GST appears to be 10 nm (6% out of a 170-nm thick GST film) thinner than the amorphous GST film due to an increase in film density by the crystallization process which results in a more compact arrangement that reduces the height of the film.

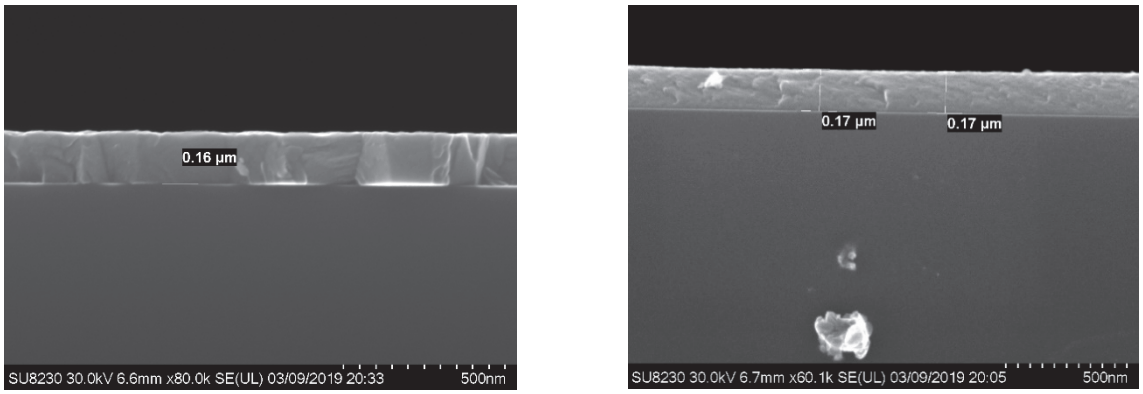

Figure 11: Cross-section View of the As-deposited (left panel) and Crystalline (right panel) GST

In our work the patterns were created by using reactive ion etching (RIE) with CHF_3/O_2 gas with a mixture ratio of 10:1 standard cubic centimeters per minute (SCCM), RF power of 150 W, and a chamber pressure of 30 mTorr. ZEP was used as a positive mask and not removed after the etching as it only slightly perturbs the overall performance. The GST and ZEP etch rates are 70 nm/min and 28 nm/min which results in the selectivity of 2.5:1. Figure 12(a) shows a trench etched in a 44-nm thick GST layer. Since dry etching can leave a relatively rough surface/sidewall, which imposes adverse effects on devices optical performances, a lift-off process is preferable for most conventional functionalities. This procedure follows standard fabrication processes with some additional constraints such as our use of Polymethyl Mathacrylate (PMMA) or ZEP. While these e-beam resists can enable thick profiles, they can

also be removed with mild dissolver liquids such as acetone without increasing the bath temperature. A flow diagram of lift-off process is shown in Figure 12(b) to clarify this process.

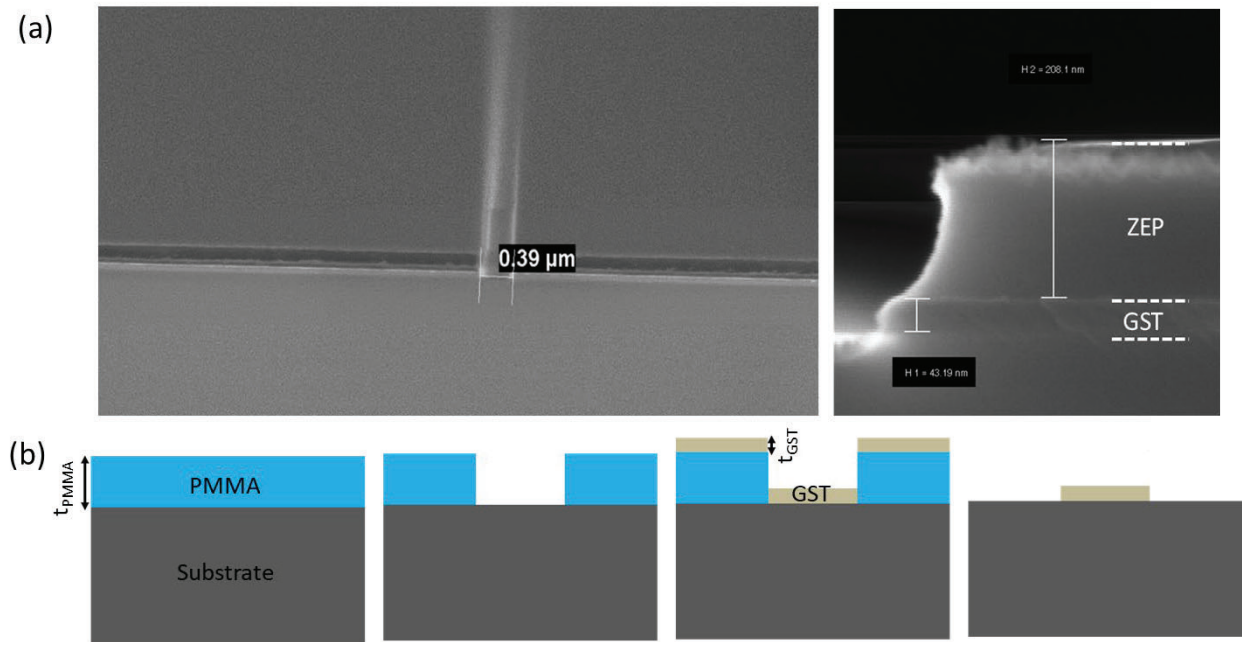

Figure 12: (a) Top and Cross-section View of a Trench Etched in a Layer of GST using ZEP as a Mask (b) Lift-off Process Flow Diagram

2.3 Multi-stage Thermal, Optical and Electrical Phase-change in GST

2.3.1 Thermal Conversion

To transform the phase of GST from amorphous to the semi- and full-crystalline, the sample under test was placed in the center of a wide hotplate at a fixed temperature of ~145ºC. The prescribed time for adding consecutive 10% crystallization level was found to be 1 minute. After heating, the sample was cooled down in the ambient environment then transferred to the optical setup for performing reflection measurements. Figure 13 shows the morphological analysis of a GST film upon the thermal switching from the amorphous to the crystalline state. The scanning electron microscope (SEM) images of the top and lateral view of the as-deposited amorphous GST film, and the lateral view of the converted sample (the GST film in the crystalline state) are shown in Figures 13(a), (b) and (c), respectively. The complex refractive index of GST thin films is determined using the Woollam M-2000 Ellipsometer and are shown in Figure 13(d).

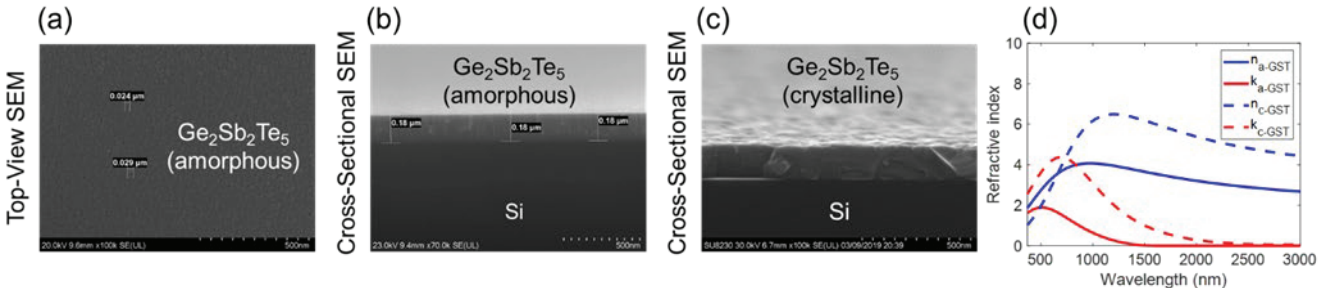

Figure 13: Morphological Analysis of a GST Film upon the Thermal Switching from the Amorphous to the Crystalline State

The SEM images regarding the (a) top and (b) lateral view of the amorphous GST, and (c) lateral view of the converted sample. (d) The measured optical properties of the GST film in its two phases.

2.3.2 Optical Conversion

Both amorphous-to-crystalline and crystalline-to-amorphous conversion of a GST film can be realized by three means: (i) a commercialized femtosecond laser setup at operational wavelength of 1064 nm (Optec WS-Flex) with a minimum spot size of 15 μm, (ii) a Nanoscribe system at an 780-nm wavelength with a minimum spot size of 1 μm, and (iii) via a Raman spectroscopy system with a 785-nm laser with a minimum spot size of 1 μm. All these tools also enable some intermediate crystalline states to be explored as shown in Figure 14. The exact composition and thickness of the GST film as well as the thermal conductivity of the medium in contact with the GST layer defines the fluence of the ultrashort pulse required for a uniform conversion. In our experiment, we found a single pulse with 6 nJ/um^{-2} is enough to successfully re-amorphize the 30-nm crystalline GST layer.

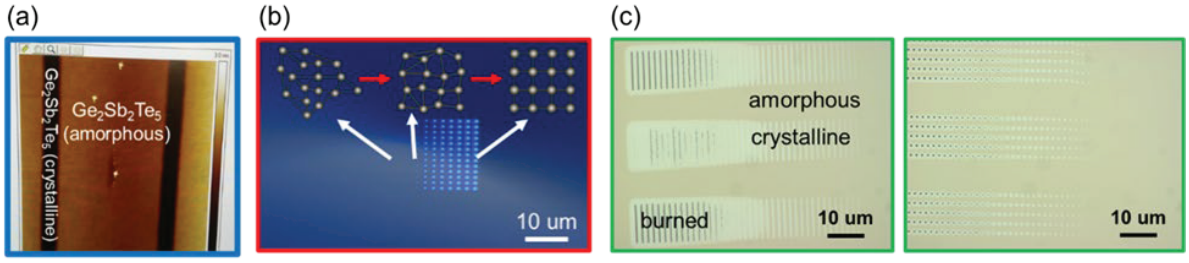

Figure 14: Crystallization and Re-amorphization of a GST thin film using (a) Optec WS-Flex, (b) Nanoscribe system, and (c) Raman system. Patterns of lines and dots with arbitrary crystallization level is achievable

2.3.3 Electrical Conversion

The success of reconfigurable PCM-based photonic platforms is entangled with the reliable control of the PCM phase, which can be reversibly switched between amorphous and crystalline states through a controlled heating process. Heating GST at a moderate temperature (150–250°C) induces a transition from an amorphous state to a crystalline one. The melting of GST at temperatures above 600°C followed by a fast cooling (>1°C/ns) enables us to convert the

crystalline GST back to its amorphous state, a process that is widely referred to as the melt quenching. The required heat for phase switching can be supplied through the direct heating or indirectly by optical and electrical stimuli. The use of direct heating, however, has been limited to preliminary proof-of-concept demonstrations as it only allows for the one-way amorphous-to-crystalline conversion. In contrast, the reversible switching of the GST phase as well as the selective conversion of individual GST inclusions have been demonstrated using the optical stimulation. However, optical stimulation necessitates bulky external laser sources and/or complex non-monolithic integration schemes, which hinder the implementation of fully integrated device platforms. Moreover, because of the low optical absorption and small absorption cross-section of amorphous GST nanostructures, recrystallization cycles require high-power optical pulses.

Electrical heating, also known as Joule heating, on the other hand, holds great promise for the ultimate miniaturization of GST-based active photonic devices, primarily because miniaturized heaters can be integrated into integrated photonics platforms. In its simplest form, Joule heating can be implemented by flowing an electrical current (I) directly through the GST film. In this scheme the large variation in the GST resistance (R_{GST}) due to differences between the amorphous and crystalline states, requires a large variation of input current to generate enough heat for the phase conversion (heat α $R_{GST}I^2$). This issue can be addressed by decoupling GST from the current path, potentially through the integration of GST on top of a µ-heater, so that the Joule heating can be controlled in the µ-heater (independent of the GST phase). Designing a µ-heater that confines the heating volume for efficient GST heating, provides a fast thermal-time-constant, and does not add optical loss is challenging. The use of metals with large optical losses should be avoided in most photonic applications. As a solution, a recent study proposed the use of graphene for designing µ-heaters with low optical loss. However, because of its defects and grain boundaries, graphene is prone to fast oxidation in the ambient environment, which makes its long-term operation under recurring heat cycles unreliable. In addition, the integration of graphene with photonics devices requires a transfer procedure that is not compatible with mainstream fabrication processes. Other reported methods such as doped-silicon µ-heaters are not holistic and cannot be adopted for alternative material systems such as SiN, silicon dioxide (SiO_2), and silicon carbide (SiC). Thus, designing a compact, low-loss, and CMOS compatible µ-heater is a major bottleneck for the integration of PCMs into photonic platforms.

Here, we develop a µ-heater platform that employs optically transparent (i.e., low loss) and electrically conductive ITO bridges for the fast and reversible switching of the GST phase between crystalline and amorphous states. By the proper selection of the electrical pulse width and amplitude we show that our platform can access virtually any intermediate crystalline state in the GST films integrated on the top of designed µ-heaters. Our estimation of energy-per-pulse consumed for the amorphous-to-crystalline phase conversion in GST is ~ 6.5 nJ in our test devices with the possibility of the sub-nJ operation in the final device configurations.

As schematically shown in Figure 15(a, b), our designed µ-heater relies on the Joule heating in a 60-nmthick ITO bridge that is electrically driven via two gold/titanium (Au/Ti) electrodes formed on its two ends. ITO is deposited by the DC sputtering of an In_2O_3/SnO_2 (90/10 wt %) target in an argon (Ar) plasma (~70 W, ~5×10^{-3} Torr). Subsequently, electrodes are formed by

the deposition of a 150/20 nm Au/Ti stack in an e-beam evaporation chamber at the base pressure of ~6×10^{-6} Torr. Finally, we integrated a 30-nm thick GST patch on top of the ITO bridge via the RF sputtering of a stoichiometric $Ge_2Sb_2Te_5$ target. Optical and SEM micrographs of the finalized devices are shown in Figure 15(c, d), respectively. The lateral dimensions of the GST patch and the ITO bridge were intentionally designed to be large for the convenient characterization of the designed platform. However, as we will show in the following sections, the dimensions can be scaled down to create miniaturized devices.

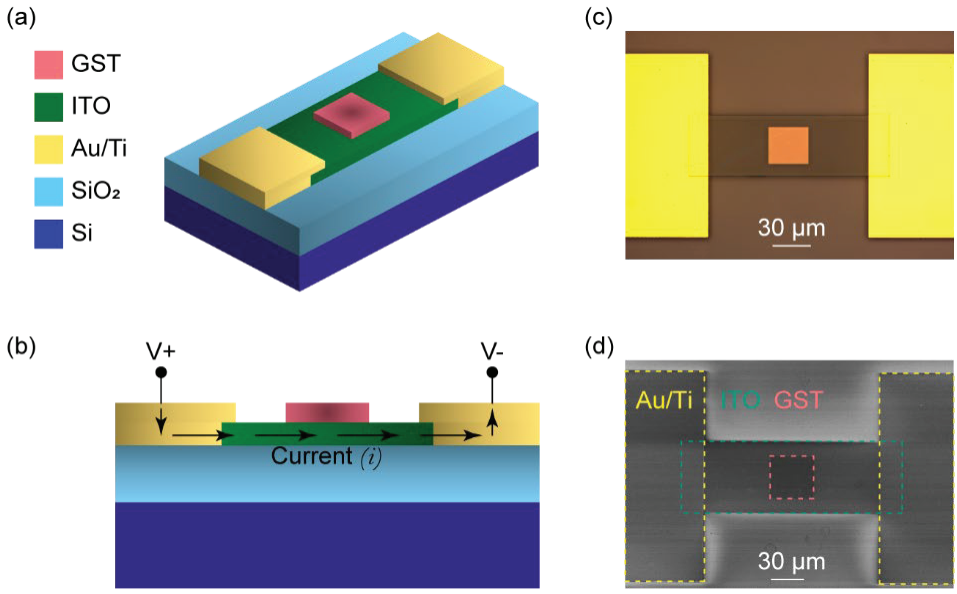

Figure 15: The Schematic Illustration of Designed μ-heaters Depicted in (a) Top and (b) Side Views. The Joule Heating in the ITO Layer Serves as the Heat Source for the Phase Conversion of the Integrated GST Patch. (c) Optical and (d) SEM Images of Fabricated Devices

The electrical conductivity of the ITO bridge is an important design parameter that directly affects the efficiency of the Joule heating. The sputtering deposition of ITO typically creates a thin film with relatively small crystalline domains, leading to a suboptimal electrical conductivity in the as-deposited films. However, the post-deposition annealing is shown to be effective for enhancing the electrical conductivity of the ITO thin films, primarily via increasing crystalline-domain sizes and activating Sn donors. Thus, we performed rapid thermal annealing ((RTA); 15 min @ 450 ºC) on our sputtered ITO, which reduced the sheet resistance of the film from ~3000 Ω/sq (before RTA) to ~100 Ω/sq (after RTA). We note that our RTA process has been conducted under a mild flow of oxygen, which, according to a previous study, reduces the optical loss of ITO thin films, a critical feature for the direct integration of our proposed μ-heater with photonic devices without the addition of extra optical loss. Furthermore, the RTA process makes the ITO bridge immune to random resistance variations during the thermal cycles required to initiate the GST phase conversion.

Before testing, we covered our device surface with a 200-nm thick SiO_2 capping layer. The role of the capping layer is threefold, it: (i) protects the GST patch from gradual oxidation in the ambient environment, (ii) prevents the decomposition of GST during the heating cycles, and (iii) it mitigates the failure of the μ-heater caused by the electric breakdown of the air at the sharp corners of the device. With the SiO_2 capping layer, (i) samples can be kept in the ambient for an arbitrarily long period of time, (ii) the GST patch can be successfully maintained during the full cycle of the amorphous-to-crystalline conversion, and (iii) the applied voltage can be increased to generate sufficient heat for the phase conversion of the GST patch integrated on the μ-heater.

For the optical characterization of this device, we primarily relied on the change of refractive index (n) and extinction coefficient (k) of GST as we electrically induced a gradual transition from the amorphous to the crystalline phase via the Joule heating of the GST patch. Thus, we used optical reflection spectroscopy to demonstrate that our proposed μ-heater enables the electrical control of the GST phase from the amorphous to the full-crystalline state with multiple intermediate states. As shown in Figure 16(a), after each Joule heating event, the reflection of a broadband light source from the center of the GST patch was collected via a 20X objective (NA ≈ 0.42) and normalized to that obtained from the ITO region without GST. The measured reflection spectra contain multiple peaks and dips, which are generated by the light interference inside the stack of layers constituting the device. The position and amplitude of these reflection features are dictated by the optical constants of various layers in the stack, among which only those of the GST layer alter upon the Joule heating events. Therefore, the modulation of peaks and dips in the reflection spectra can be used for the back-calculation of the optical constants of the GST layer, providing an effective means for estimating the crystalline phase of the GST layer after each Joule heating event.

To extract the degree of crystallization from the measured reflection spectra we need to benchmark the estimated n and k values against a reference data set. Thus, following previous reports, we vacuum annealed an amorphous GST layer at ~ 250ºC for 5 mins, which provides a reference sample for the crystalline state of GST. Subsequently, we used ellipsometry measurements with a Tauc–Lorentz dispersion fitting to directly obtain n and k values for the reference crystalline/amorphous GST films as depicted with solid lines in Figures 16(b) and (c), respectively. To obtain similar references for the intermediate states of GST, we used an effective-media approximation in which a fraction (α) of the GST volume is assumed to be in the crystalline state and the remainder (1-α) in the amorphous state such that ($0 < \alpha < 1$). Thus, using the measured n and k values of amorphous (i.e., $\alpha = 0$) and crystalline (i.e., $\alpha = 1$) GST films, we can extrapolate n and k values for any arbitrary intermediate GST state using the Lorentz–Lorenz equation as follows:

$$\varepsilon_{eff}(\alpha) = \frac{1+2T}{1-T}, \qquad T = \alpha \frac{\varepsilon_c - 1}{\varepsilon_c + 2} + (1-\alpha) \frac{\varepsilon_a - 1}{\varepsilon_a + 2} \qquad \text{Eq. (1)}$$

$$n_{eff}(\alpha) + ik_{eff}(\alpha) = \sqrt{\varepsilon_{eff}} \qquad \text{Eq. (2)}$$

In Eq. (1), the α-dependent dielectric constant of the effective medium (ε_{eff} (α)) can be calculated from the dielectric constants of the crystalline (ε_c) and amorphous (ε_a) GST states. Subsequently, the real (n_{eff}) and imaginary (k_{eff}) parts of the effective refractive index can be

derived from the ε_{eff} (α) by using Eq. (2). Some of the extrapolated n and k values for intermediate GST states with α ≠ 0, 1 are plotted with dashed lines in Figures 16(b) and (c).

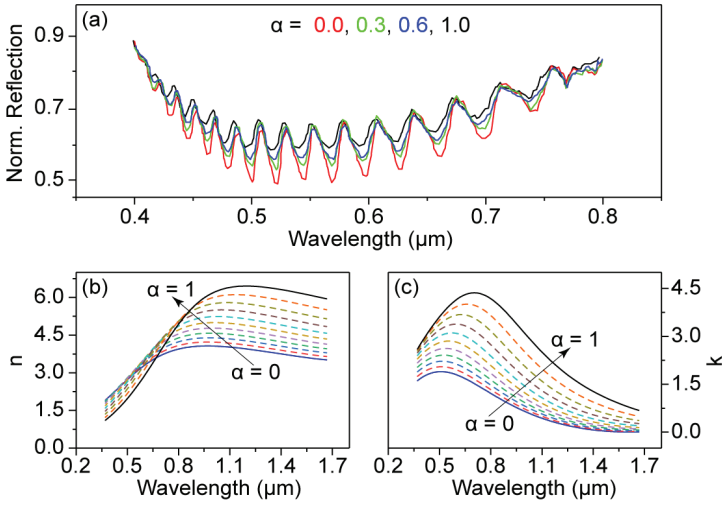

Figure 16: Optical Reflection Spectra of the GST/ITO/SiO2/Si Stack Normalized to that of the ITO/SiO2/Si Stack (a). The Crystallization Degree (i.e., α) after each Joule Heating Event is Extracted using the Transfer-matrix Method (see SI for details). As explained in the main text, an Effective-media Approximation is assumed for the Optical Constants of GST layer. (b, c) Refractive Index (n) and Extinction Coefficient (k) of GST, Respectively, at fully Amorphous (i.e., α = 0), fully Crystalline (i.e., α = 1), and Nine Intermediate States with 0.1 Incremental Steps

The solid lines represent data experimentally measured by spectroscopic ellipsometry. Dashed lines are extrapolated using the Lorentz–Lorenz equation as explained in the main text.

To estimate the crystallization level after each Joule heating event, we employed the transfer-matrix method to regenerate the experimental reflection spectra shown in Figure 16(a). In our calculations, we used $n_{eff}(\alpha)$ and $k_{eff}(\alpha)$ as the optical constants of the GST layer, and, following a brute-force approach, we swept the α parameter from 0 to 1 and looked for the best fit to the experimental results. Our calculations showed that the reflection spectra displayed in Figure 16(a) can be successfully fit with α = 0, 0.3 ± 0.1, 0.6 ± 0.1, and 0.9 ± 0.1. We also note that the optical spectra shown in Figure 16(a) were measured when the μ-heater was switched off after each heating step, which exhibits the nonvolatile nature of induced changes in GST. Our results clearly demonstrate that our designed ITO μ-heater enables nonvolatile manipulation of the GST phase via the controlled Joule heating.

The change of the GST phase can be further studied through monitoring its electrical properties, especially for miniaturized dimensions at which optical characterizations are complicated. As shown in Figure 17(a), we designed a four-electrode device in which two readout electrodes were placed across the GST patch for the electrical characterization of the phase following sequential Joule-heating pulses applied to the ITO μ-heater. To electrically isolate the GST from the underlying ITO film, a 10-nm thick HfO_2 spacer layer was deposited between the GST patch and the ITO μ-heater. For the amorphous-to-crystalline conversion, we applied 200-ms voltage pulses of varying amplitudes to the μ-heater, and after each pulse we measured the GST

resistance (R_{GST}) using the readout electrodes. As shown in Figure 17(b), with an increasing voltage and number of applied pulses, the GST resistance monotonically drops while following staircase profile as expected. This identifies that the GST phase gradually changes from the amorphous state (high-resistance) to the crystalline state (low-resistance). Indeed, each distinguishable R_{GST} value represents a different GST phase, showing that GST can be configured in virtually any intermediate crystalline state through the controlled excitation of the ITO μ-heater. However, the impact of the pulse amplitude on changing the GST phase is more significant than the number of applied pulses. In fact, at a fixed pulse amplitude, the minimum achievable resistance saturates with the number of applied pulses. This observation suggests that the crystallization of GST is primarily a temperature-driven phenomenon and obtaining higher crystallization levels mandates the temperature increase via the application of an electrical pulse with a larger amplitude.

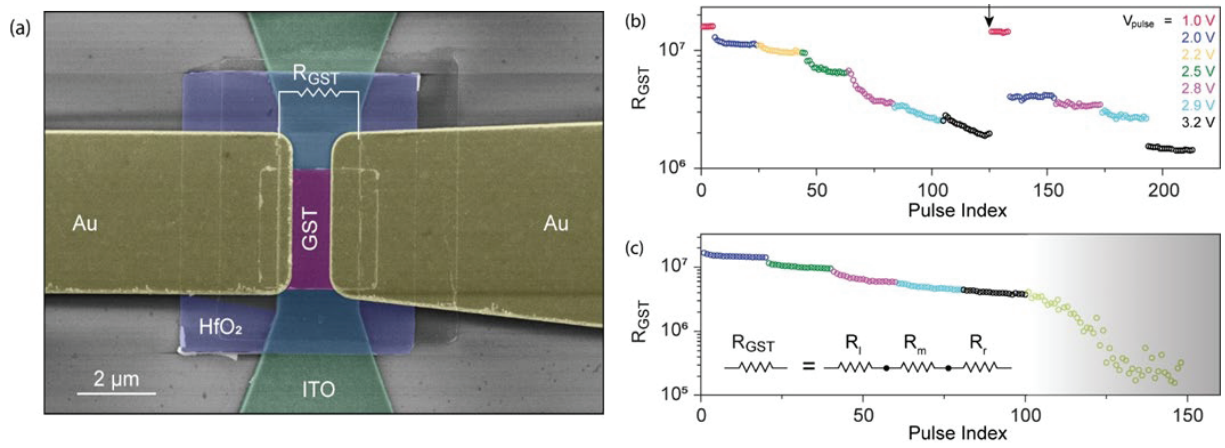

Figure 17: False-colored SEM Image of the Device (a). The GST Phase is changed through the Joule Heating in the Underlying ITO Layer and Monitored by the Measurement of RGST between the Au Contacts (b). Inset: the Measured RGST is composed of Two Side Segments Close to the Left and Right Electrodes (Rl and Rr) and a Middle Segment (Rm) (c)

The GST resistance as a function of the number and amplitude of voltage pulses applied to the ITO heater. All pulses are 200-ms wide. The arrow highlights the re-amorphization of GST by the application of a short voltage pulse (width: 50 ns, height: 20 V) to the ITO μ-heater. As explained in the text, Joule heating in ITO (i.e., the unshaded part of panel c) primarily affects R_c. The side segments can be affected by the application of current pulses to the Au electrodes (shaded region). The width and height of the current pulses are 200 ms and 200 μA, respectively.

The GST phase can be switched back to the amorphous state by melt-quenching, a process that requires the high-temperature melting followed by a rapid cooling of the crystalized GST to return it to its amorphous state. Thus, we increase the amplitude of the voltage pulse to ~9 V, for melting, and narrow the pulse width down to 50 ns for the fast cooling. As indicated by an arrow in Figure 17(b), the application of a short pulse to the μ-heater successfully resets the GST resistance back to the amorphous level, which verifies the feasibility of reversible switching in our developed ITO-based μ-heater platform. Interestingly, the re-crystallization of the

melt-quenched GST displays a sudden drop in resistance, which is then followed by the recovery of the stepwise resistance drop in the subsequent crystallization steps. In other words, the number of achievable intermediate crystalline states in the melt-quenched GST is less than that in the as-deposited amorphous film. Previous studies suggest that such a difference stems from the residual crystalline domains in melt-quenched GST films, which bypasses the nucleation step that is required for the crystallization of as-deposited GST films. Therefore, compared to as-deposited films, an accelerated crystallization is anticipated in melt-quenched GST films. Nevertheless, our platform offers reversible switching of the GST phase with multiple intermediate crystalline states in a repeatable way. We note that subsequent crystallization cycles (not shown here) follow the trend observed in the second cycle, hinting that a pre-conditioning step is required prior to the long-term operation of the device.

Our demonstrated resistance contrast upon the phase transition is slightly larger than one order of magnitude, which is noticeably smaller than the expected two-orders-of-magnitude change, as reported elsewhere. We attribute this discrepancy to the heat-sinking effect of the metallic electrodes used for the readout of the GST resistance. The overlap of these metallic electrodes with the ITO bridge disturbs the otherwise-uniform heat profile of the μ-heater and creates two locally cold regions close to the left and right metallic electrodes, which leaves behind two amorphous segments on the sides of the central crystalline GST segment. In other words, the measured resistance (i.e., R_{GST}) is composed of the serial connection of three components: two residual amorphous segments at the vicinity of the left and right electrodes (i.e., $R_{left\text{-}am}$ and $R_{right\text{-}am}$) and a middle segment (i.e., R_{middle}) that can be switched between amorphous and crystalline states; that is, $R_{GST} = R_{left\text{-}am} + R_{middle} + R_{right\text{-}am}$. Therefore, the smallest achievable resistance in the crystalline state is $R_{GST} = R_{left\text{-}am} + R_{middle\text{-}crys} + R_{right\text{-}am} \approx R_{left\text{-}am} + R_{right\text{-}am}$, which limits the attainable resistance contrast. These residual amorphous segments, however, can be crystallized by the direct flow of electrical current through the Au electrodes for the local Joule heating at the vicinity of the readout electrodes. As shown in the shaded region of Figure 17(c), following the sequential application of current pulses (200 μA, 200 ms) to the Au electrodes, the GST resistance can be further reduced by an additional order of magnitude to achieve an overall of two-orders-of-magnitude resistance contrast.

2.4 Miniaturized Integrated Photonic Phase Shifters Using the Hybrid SiN/GST Platform

We performed a systematic study of the proposed hybrid SiN/GST platform for the reconfigurable integrated photonic devices, especially phase shifters with the final goal of designing the miniaturized electrically controllable phase shifters. To enable the accurate characterization of the optical propagation phase at different crystalline stages of GST, we primarily used Mach-Zehnder interferometers (MZI) and racetrack-resonator-based add/drop filters in which, one waveguide arm is used for phase shifting through changing the crystalline state of GST. Since SiN has a mild thermo-optic effect, we fabricated a ring resonator in the structure whose resonance shift can be attributed to environmental changes to compensate for such effects. Figures 18(a) and (b) show the schematic and microscope image of a typical add/drop structure used for our investigations. Due to the different complexity levels of thermal, optical, and electrical GST phase change, we started with the thermal mechanisms and moved to optical, and finally, electrical means of reconfiguration. The lessons learned in the thermal and optical conversion experiments were very helpful in the final demonstration of the electrically

controlled phase shifters with the unprecedented level of miniaturization, as a major breakthrough of this research.

2.4.1 Thermally-controlled Phase Shifters

The first step of device demonstration was based on direct heating of the device using a thermally controlled stage. The add/drop device in Figure 18(b) was heated at 150ºC for different times, and the response of the devices was measured and corrected using the response of the on-chip ring resonator. The resonance wavelength of the racetrack resonator in the add/drop architecture was modified by the GST-based phase shifter. The measured transmission spectra for different stages of GST conversion (corresponding to the successive heating periods at 150ºC) are shown in Figure 18(c). The response with the highest extinction ratio corresponds to the amorphous GST, and that with the lowest extinction ratio corresponds to the fully crystalline GST. The intermediate stages are all repeatedly achieved. Figure 18(d) shows the more explicit data obtained from the analysis of the transmission data in Figure 18(c) in terms of optical phase and linewidth (this also shows the effect of loss). It is clear that by using a subwavelength GST patch (length: 0.9 μm), a large phase shift of 85º was achieved. Achieving a similar phase shift in a typical Si or SiN waveguide requires devices orders-of-magnitude larger.

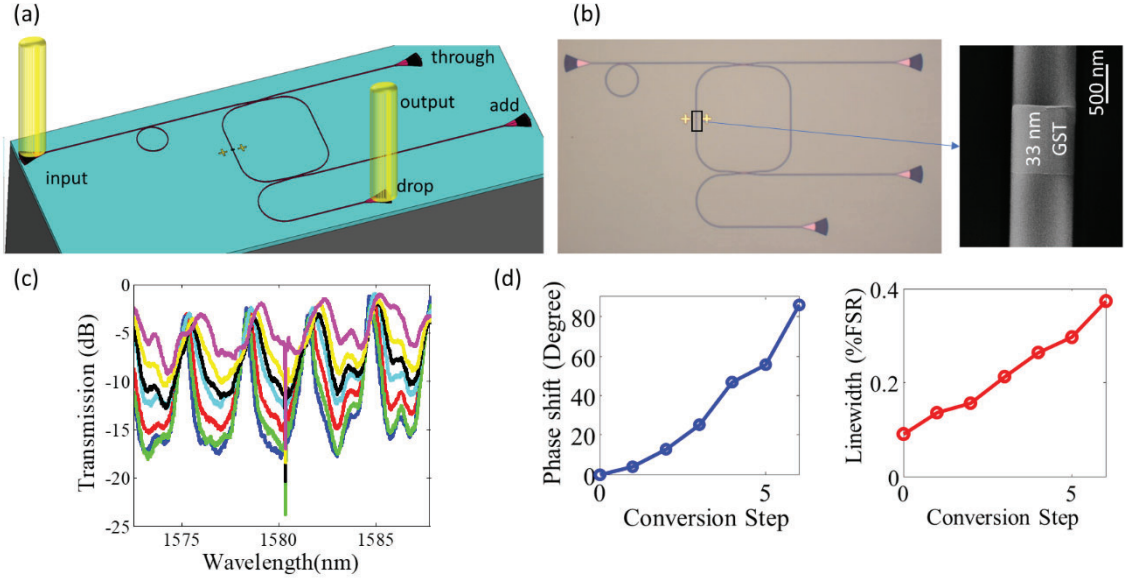

Figure 18: The Schematic of a Reconfigurable SiN Resonator-based Add-drop Filter Enabled by a GST-based Phase Shifter (a). Bright Field Image of the Fabricated Device Phase-shifter (b). The Microring Resonator (after the input port) is considered as a Reference to Avoid Thermal Compensation Process in Successive Measurement of the Intact and GST-loaded Device. The Height and Width of the SiN Waveguide are 400 and 1500 nm, respectively. Inset: SEM Image of the GST-based Phase Shifter. The Transmission Spectra from the Drop Side of the Device for 7 Different Material States of GST achieved by Uniformly Heating the Sample at 150oC with Different Amounts of Time (c). Corresponding Phase Shift and Linewidth for Different Crystallization Levels. Note that an 85 o Phase Shift (with respect to the initial state) is Achieved after Full Crystallization of the GST Section (d)

To achieve higher levels of phase shift, we designed another phase shifter with a larger GST section and tested it using the MZI structure shown in Figure 19(a). The transmission spectra in Figure 19(b) show the as-grown (amorphous) GST and two other GST phase states with optical phase shifts of 179° and 214°. These structures were carefully studied to obtain a good understanding of the number of achievable GST crystalline phases and their consequences on the optical phase shift to facilitate the final design of the practical phase shifters with electrical reconfiguration.

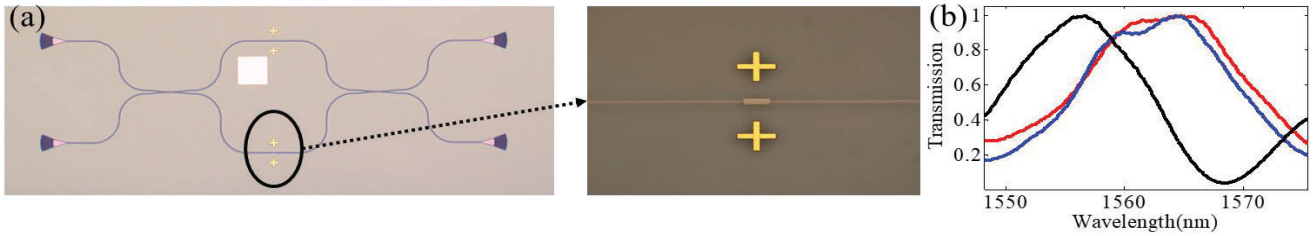

Figure 19: Microscope Image of a Reconfigurable MZI with a SiN/GST Phase Shifter (a). The Zoomed-in Image Shows the GST Section (1.5 μm by 3 μm) on the SiN Waveguide. (b) Measured Transmission for the Device in (a) with different Crystalline States of GST, where Black, Blue, and Red Curves Correspond to As-grown (amorphous), Partially Crystalline, and Fully Crystalline States the Calculated Optical Phase Shifts for the Blue and Red Curves are 179° and 214°, respectively

While the repeatable results in Figures 18 and 19 prove the feasibility of achieving miniaturized phase shifters using multi-stage GST crystallization, direct heating cannot be used for forming practical devices. Unfortunately, the re-amorphization of the GST section through direct heating at 650°C with a sharp heat pulse is not easily feasible. In these experiments, the re-amorphization was performed in a separate oven. Nevertheless, these initial results are very promising for making practical devices using other means of GST phase conversion.

2.4.2 Optically-controlled Phase Shifters

To enable integrated photonics phase shifters incorporating GST, we used two types of structures: (i) symmetrical/asymmetrical MZI-based phase shifters, and (ii) resonator-based phase shifters. Figure 20 (a) shows the schematic representation of a symmetric MZI with a GST-based phase shifter in which two large micro-scale GST sections are deposited on top of the upper and lower waveguide branches. The microscope image of the fabricated reconfigurable SiN MZI with a 1.5-μm GST section is shown in Figure 20(b). Converting the lower GST section from its as-deposited low-loss amorphous state to the higher-absorption crystalline state, the propagating wave transmitted through the bottom branch experiences different effective refractive indices, which leads to a damping effect in the transmitted power (see Figure 20(c)) and more interestingly, a phase shift at the output port. The multi-level (up to 3) conversion of the micro-scale GST section was performed using the pulsed laser of a Raman system with an operational wavelength of 488 nm and 1-mW power, and a maximum phase shift of 19° was achieved.

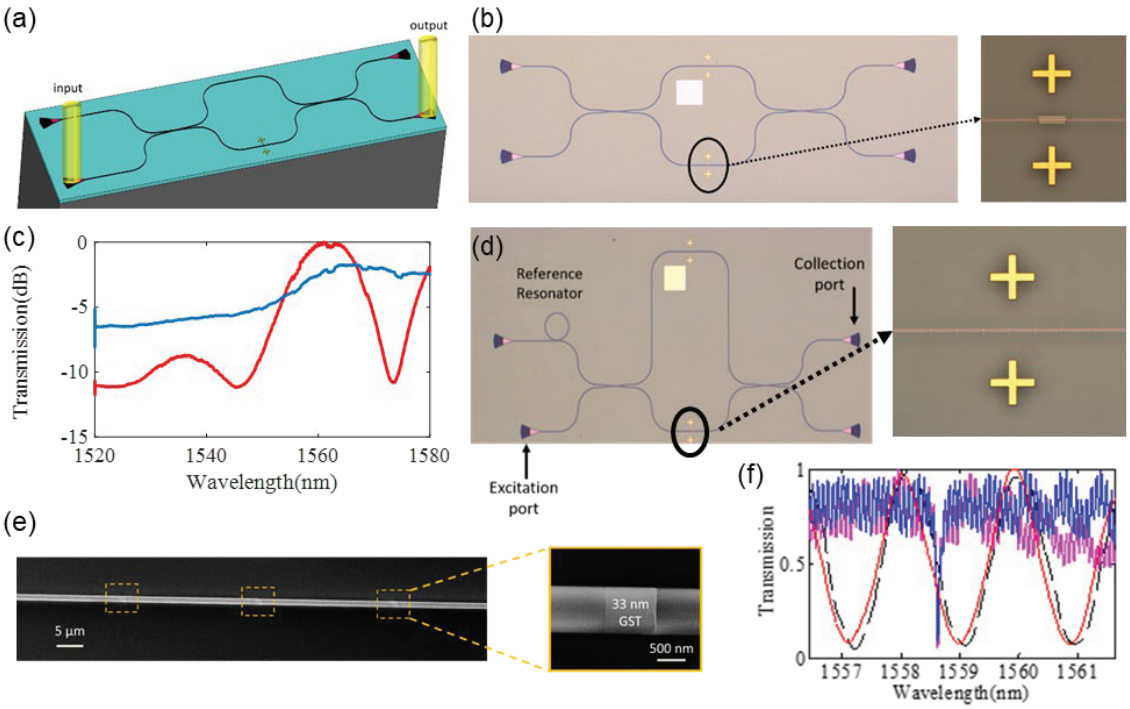

Figure 20: Schematic Representation of a Reconfigurable SiN Symmetric Mach-Zehnder Interferometer (MZI) with a GST-based Phase Shifter (a). Bright Field Image of the Fabricated Symmetric MZI with the Large GST Square as a reference to Measure the Reflectance after Full Conversion Process (b). The Height and Width of the SiN Waveguide are 400 and 1500 nm, respectively. Inset: Large View of the 3-µm x 1.5- µm GST Section Located on Top of the Lower Branch of the MZI. The Transmitted Power at the Output of the MZI for Amorphous (red line) and Crystalline (blue line) GST (c). Bright Field Image of the Fabricated Asymmetric MZI with 7 Sub-micron GST Sections Deposited on top of each Branch (d). The SEM Image of the MZI shown in (d) and the Nanoscale GST Patch in inset (e). The Transmission Spectrum of the MZI for three different Material States of GST (f)

For conversion of GST from the initial as-deposited to the intermediate states, the sample was located in a Raman system and was illuminated by appropriate optical pulses from a 488 nm laser with 1 mW of average power.

To increase the degrees of freedom to achieve finer tunability, we designed the phase shifter shown in Figure 20(d) with 7 sub-micron-scale GST sections on top of each branch of an asymmetric MZI so that we can convert a certain number of GST sections to obtain an accurate phase shift. Figure 20(e) shows the SEM image of three of these patches each with size of 33 nm. The measured transmitted power at the output port in Figure 20(f) shows the fine tunability of the phase shift over the telecommunication wavelengths. To achieve a full 180 ^{o} phase shift, we employ repeatable multi-stage phase conversion of the GST section using pulsed laser light at 488 nm in a MZI-based device shown in Figure 21(a) in which 10 sub-micron GST sections are deposited on top the upper waveguide. While converting all the GST patches results in a full 180^{o} phase shift of the transmitted wave, partial conversion of the GST patches enables us to finely tune the phase shift, as shown in Figure 21(b).

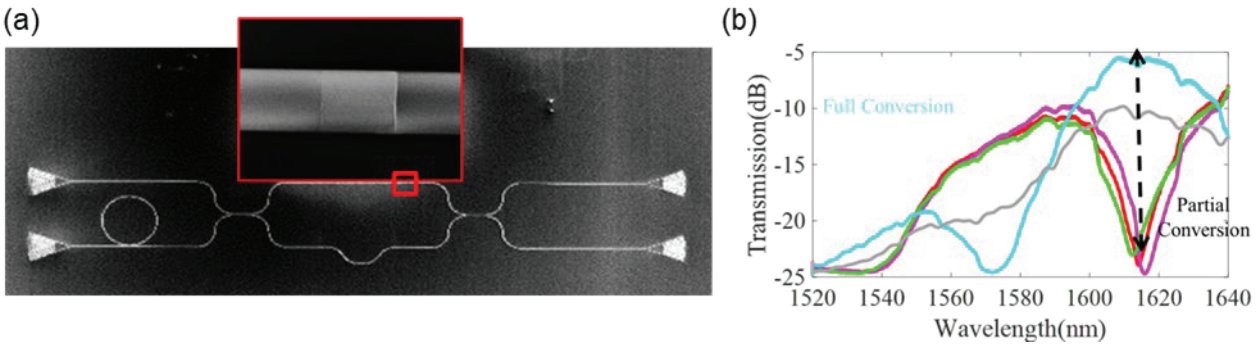

Figure 21: Optical Conversion with Multi-stage GST

The SEM image of the fabricated asymmetric MZI-based phase shifter with 10 sub-micron GST sections deposited on top of the upper branch (a). The measured transmission response at the output port demonstrating the minute and full 180º phase shit achieved by partial and full crystallization of the GST sections, respectively (b).

More interestingly, we designed and fabricated multiple coupled-ring resonators in a MZI-based configuration (see Figure 22(a)) to enable both multi-stage phase shifters and a multi-channel switch. In this case, the switching of each channel is based on a coupled-resonator architecture with one resonator having 3 GST patches with different dimensions on top (labeled by GST_1 and GST_2 in Figure 22(a)). By selectively converting certain GST patches (the two GST_1, the single GST_2, or both), we realized selective switching of intended channels as shown in Figure 22(b). Again, the conversion of the GST sections was performed by using the pulsed laser beam of the Raman system with 488 nm operational wavelength and 1 mW of average power.

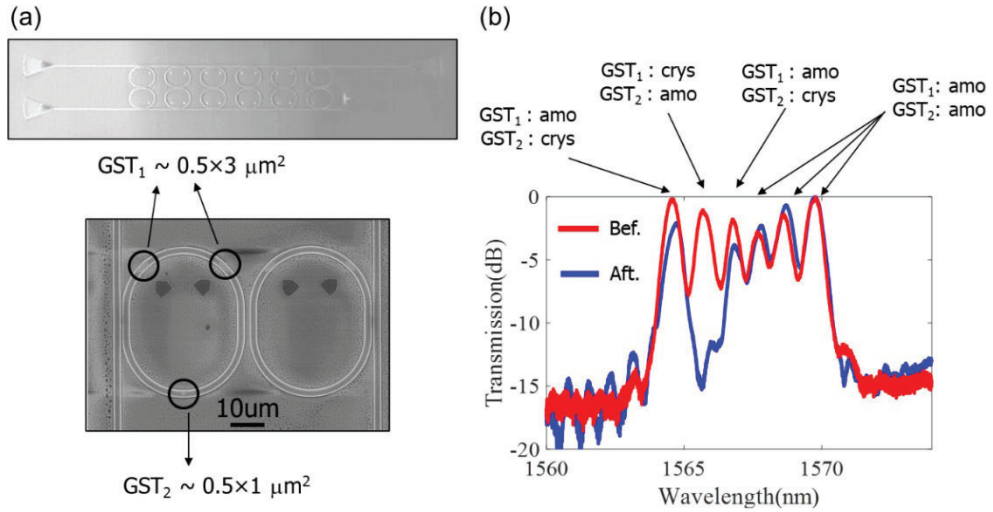

Figure 22: Selective Switching of Intended Channels in a Coupled-resonator Switch Bank

(a) The SEM image of the fabricated device consisting of multiple coupled resonators with multiple GST patches deposited on top of each, which can be selectively converted by laser pulses. The bottom SEM shows the zoomed-in version of the coupled resonators for each wavelength channel. (b) The transmitted power at the output port showing the selective switching operation. The crystalline state of GST1 or GST2 sections for each channel before and after conversion are shown (amo: amorphous, crys: crystalline). Conversion of the larger sections (GST1) has a more pronounced effect as expected.

2.4.3 Electrically Controlled Phase Shifters

We integrate our hybrid GST/ITO platform on top of a SiN waveguide, where the phase and amplitude of the optical transmission can be modulated by adjusting the GST crystalline state between the fully amorphous and fully crystalline phases. The SiN waveguide here is fabricated using a 400-nm thick SiN film deposited by low-pressure chemical vapor deposition (LPCVD). The waveguide width is set to ~ 1400 nm to ensure single-mode operation around the wavelength of 1550 nm. The geometry of the GST nanostructure is tailored to optimize the ratio of the optical phase shift to the transmission loss upon the full conversion from the amorphous to the crystalline state, while maintaining a very small spatial footprint. The geometry of the ITO is also designed to enable a uniform temperature profile across the GST section, rapid thermal reconfiguration, while also minimizing the optical loss caused by the integration of the ITO μ-heater. The electrical connections to the ITO bridge are supported by two small SiN sidebars (width ≈ 500 nm), which enable a low-resistance electrical connection to the ITO μ-heater with minimal extra waveguide loss (< 0.2 dB). The thickness of the ITO and GST layers are 60 nm and 30 nm, respectively.

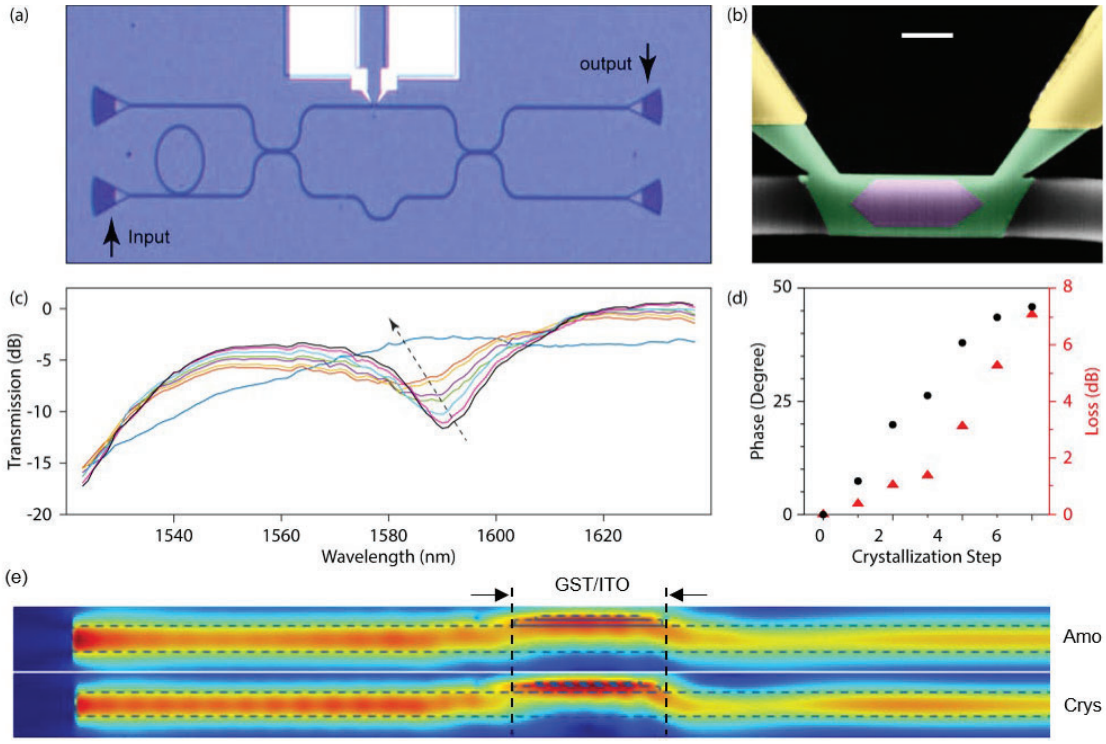

Figure 23: Optical Image of a MZI Phase Shifter Fabricated in a SiN Platform (a). Input and Output Ports are identified in the Image. The Ring Resonator is used for the Calibration Purpose (b). The False-colored SEM Image of the GST/ITO Segment Integrated on the Upper Arm of the MZI. GST, ITO, and Au Layers are Colored Purple, Green, and Yellow, Respectively. Scale Bar Represents 0.5 µm. The Optical Transmission (i.e., from input to output) for Several Crystalline States of GST (c). Arrow Points from Amorphous to the Crystalline State. Extracted phase shifts and optical loss for each crystalline State of the GST (d). The FDTD Simulation of the Electric Field Profile along the SiN Waveguide for Amorphous (top) and Crystalline States of the Integrated GST Section (e)

The field overlap with the GST section increases following the crystallization of GST. Field profiles are separately normalized for amorphous and crystalline states.

To characterize the phase and amplitude changes upon the GST conversion, we integrated the designed phase shifter into the arms of an MZI structure. Figure 23(a) and (b) show the optical image of the fabricated MZI and the false-colored SEM image of the GST/ITO µ-heater integrated on top of the SiN waveguide. To characterize the device, we measured the transmission spectrum of the MZI at various GST crystalline states. In this case the GST conversion is induced by exciting the ITO heater following a train of voltage pulses where the crystalline state of the GST can be controlled by adjusting the amplitude, width, or number of the applied pluses as discussed before. Figure 23(c) shows the transmission spectrum of the MZI under the application of voltage pulses to the ITO µ-heater. The spectral shift and increased asymmetry in the spectral features of the MZI response are indicative of the amplitude modulation and phase shift in the waveguide induced by the nonvolatile change of the GST crystalline state. Figure 23 (d) shows the extracted phase shift and amplitude of the integrated

waveguide versus the applied voltage. The GST nanoparticle provides a reconfigurable phase shift from 0 degree to 50 degrees; however, the phase shift is accompanied by a relatively large transmission loss of ~ 7dB.

We used the finite-difference time-domain (FDTD) tool in the Lumerical simulation package to study the overlap of the electric field of optical signal, inside the SiN waveguide, with different phases of the GST nanoparticles (Figure 23(e)). The optical constants of the GST and ITO materials were extracted from ellipsometry measurements. Our calculations show that the integration of our designed μ-heater platform with the SiN waveguide results in a relatively low loss of ~ 0.2 dB at the target operation wavelength (1550 – 1600nm). Additionally, the as-deposited GST film (i.e., amorphous phase) contributes an additional loss of less than 0.6 dB, which is due to a combination of the optical absorption in GST film and the scattering loss caused by the large refractive index of GST as compared to the SiN waveguide. As Figure 23(e) shows, following the GST crystallization, the overlap of the electric field with the GST segment increases, which leads to the modulation of the phase and amplitude of the optical signal inside the SiN waveguide. Such an enhanced field overlap and phase/amplitude modulation stem from the larger refractive index of the crystalline GST as compared to the amorphous GST. We also note that the small refractive index contrast between SiN and ITO extends the electric field from the SiN waveguide into the ITO layer, which enhances the field interaction with the GST film on top of the ITO layer.

2.4.4 Performance Measures of the Proposed Miniaturized Phase Shifters

For a better estimation of the performance of the demonstrated phase shifter, we first study the spatial and temporal temperature profiles in response to the voltage pulses applied to the ITO μ-heaters. To do so, we solved electro-thermal equations using the COMSOL Multiphysics simulation package for the experimental condition explained in Figure 17. As shown in Figure 24(a), despite some expected temperature drop across the ITO width, the temperature profile is spatially uniform along the ITO bridge, suggesting that a GST section located at the center of the μ-heater can be uniformly switched between amorphous and crystalline states. In addition to the spatial temperature uniformity, our designed platform ensures the fast thermal dynamic needed for the re-amorphization of crystalline GST. As shown in Figure 24(b), a cooling rate of ~ 1.3^{o}C/ns is achievable following the trailing edge of a 50-ns voltage pulse, close to the reported value of 1^{o}C/ns for the melt quenching of crystalline GST. A similar thermal transient simulation for the amorphous-to-crystalline phase conversion is also presented in Figure 24(c), showing that a 3-V pulse with a 300-ns width can elevate the GST temperature to ~ 350 ^{0}C thus enabling the full crystallization of an amorphous film.

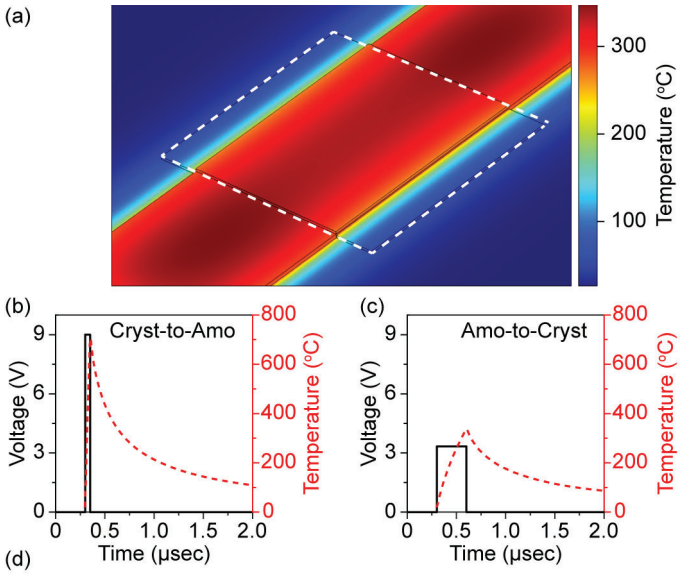

(d)

	Pulse Amplitude (V)	Pulse Width(ns)	Peak Power (mW)	Energy per Pulse (nJ)
Amo-to-Cryst	< 3	300	22	6.6
Cryst-to-Amo	~ 9	50	202	~10

Figure 24: The Spatial Heat Profile across the Hybrid ITO/GST Device Plotted at the end of a 300-ns Electric Pulse with a 3-V Amplitude (a). Dashed Lines Outline the GST Section. Geometrical Dimensions are Similar to those shown in Figure 17 without readout Electrodes. Temporal Heat Profiles (dashed lines) Generated by the Voltage Pulses (solid lines) Applied to the ITO μ-heater for Amorphous-to-crystalline and Crystalline-to-amorphous Phase Switching, respectively (b, c). A Summary of the Pulse Condition and Power/Energy Consumption for the Revisable Switching of the GST Phase (d)

For these calculations, the ITO resistance was measured to be 400 Ω.

Combining the experimental results of Figure 17 with the electro-thermal simulations of Figure 24, we can estimate the performance measures of our proposed platform. As tabulated in Figure 24(d), the energy per pulse needed for the crystallization of the amorphous GST and the amorphization of the crystalline GST are ~ 6.6 nJ and 10 nJ, respectively. However, we note that these values are overestimated, and the real energy consumption in an actual device (i.e., not a test device) is noticeably smaller because of two main reasons. First, the readout electrodes, used in the test device, sink a portion of the generated heat that could be otherwise consumed for the phase conversion in GST. Second, the HfO_2 layer, used for the electrical isolation of the ITO bridge and readout electrodes, adds a thermal barrier between the ITO and the GST. Thus, the generated heat in the ITO μ-heater may not be fully delivered to the GST section during the short voltage pulses employed for the phase conversion. The elimination of these two factors can potentially lead to the sub-nJ power consumption in our hybrid ITO/GST platform.

2.5 Outlook: New Potential Breakthroughs Enabled by the Proposed Platform

This two-year research enabled us to create a new platform, which should have a transformative impact for a number of photonic solutions seeking to address a large range of applications. The following summarizes some of the potential directions that could be the base for follow-on programs.

2.5.1 Reconfigurable Integrated Photonic Devices for Visible-IR Ranges

Despite extensive development of integrated photonic devices and systems, the issue of reconfigurability [i.e., using the same device/system to perform different functionalities, e.g., filtering, pointing (LiDAR), switching, etc.] at reasonable speeds and power consumptions is still a major challenge. More importantly, most devices and systems operate at a limited range of IR wavelengths (e.g., 1.3–1.6 μm). On the other hand, the realization of reconfigurable integrated photonic devices in the visible range is urgently needed for emerging applications in many new areas such as quantum information processing, sensing, and visible-light LiDAR. While SiN is an excellent CMOS-compatible material, its dielectric nature hinders the formation of such devices. PCMs can provide the active (and strong nonlinear) optical properties that SiN lacks. The large refractive index change of PCMs, their non-volatility, and the reconfiguration times (100's ns) perfectly match or surpass the required performance for several emerging applications. The integration of multiple PCM nanostructures on waveguides or resonators and the ability to individually control them will provide a rich platform to create reconfigurable phase shifters, delay lines, switches, routers, filters, and channelizers just to name a few sub-systems that can benefit from this capability. This will be extremely valuable and timely for applications in visible and near-IR wavelengths in which a universal active and nonlinear material platform is still needed. The new advances in quantum applications, especially in the interaction of photons and atoms/ions in a miniaturized chip in the 400–800 nm wavelength range further necessitates such a universal platform. The multi-MHz speed of the PCM-based devices will be sufficient for several quantum applications of interest (e.g., following the motion of a trapped atom/ion in a quantum chip). As such, the PCM-based platform can be of great value to existing DARPA projects like LUMOS or A-PHI. Figures 25(a)-(c) show some of our fabricated structures in the hybrid platform, and Figure 25(d) shows the architecture of the unit cell of a reconfigurable filter that can be enabled by the proposed platform.

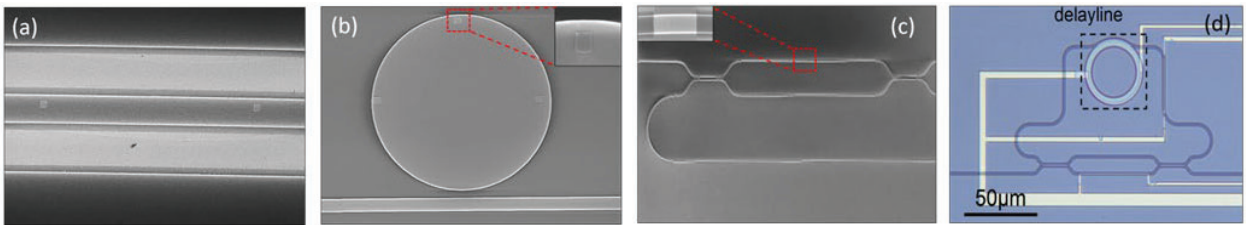

Figure 25: Proposed Building Blocks and Functional Integrated Nano-photonic Devices
Reconfigurable waveguide (e.g., as a multi-level phase shifter) (a), unable resonator (for modulation, phase shifting, delay) (b). Reconfigurable interferometer (for analog modulation and switching) (c), and low-order reconfigurable filter (d). The phase change in the integrated PCM nanoparticles (individually or as an array) result in reconfiguration of the device operation.

2.5.2 Chip-based Optical Beam-formers and Scanners

Integrated photonics has a great potential to miniaturize the existing bulky systems for light-matter interaction and even provide new approaches for such interactions (especially the photon-atom/ion interaction in quantum systems and photon-neuron interaction in brain probing). A key enabling functionality is converting the on-chip waveguide mode to a free-space beam with the required spatial and spectral pattern to interact with the material system outside the chip. More importantly, the spatial-spectral mapping must be dynamic and therefore reconfigurable in microseconds to mitigate any unwanted displacement of the material system (e.g., trapped atom/ion). The ability to also receive and process the emitted or reflected signal from the outside material is another potential advantage of photonic chips for light-matter interaction. Conventional gratings cannot provide all these required functionalities. While recent advances in metasurfaces (MSs) claim to address the shortcomings of these gratings, their meaningful reconfiguration at the subwavelength dimensions requires large refractive index changes which are not easily implemented. As a result, a major breakthrough can be enabled by integration of MSs with PCMs. As such, the proposed light-matter-interaction chips can act as highly specialized LiDARs that can steer the beam dynamically to follow the motion of the atoms/ions above the chip with an optimal beam with the desired spatial-spectral pattern (e.g., multi-wavelength focus) over a wide wavelength range (as needed by the atomic physics community). Such a platform could provide new dimensions in quantum photonic chips for sensing (e.g., atomic clocks, magnetometers, electrometers, and gyros) that are already being investigated through different DARPA programs (e.g., DARPA A-PHI). Figure 26(a) shows the schematic of the proposed platform, and Figure 26(b) shows its application for an atom/ion chip for quantum sensing applications.

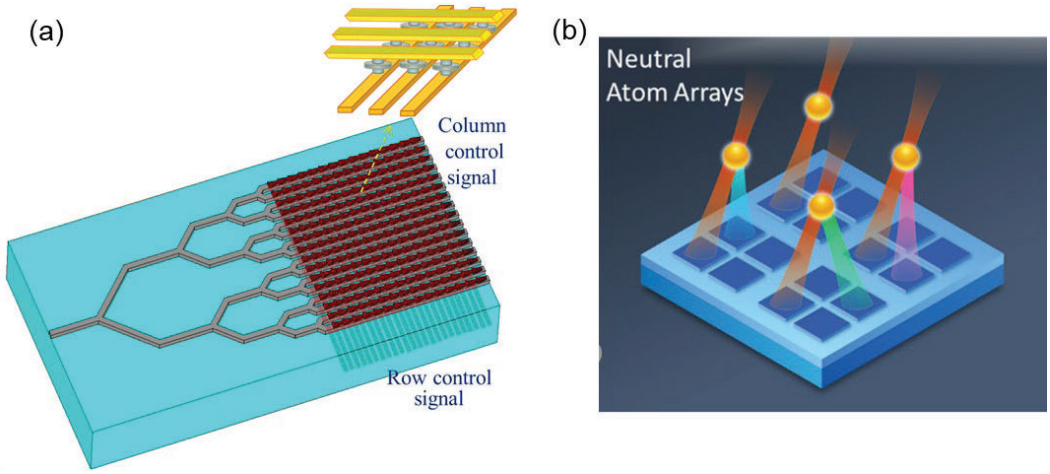

Figure 26: Schematic Representation of a Two-dimensional Phased Array Structure as the Building Block of a Reconfigurable Metasurface (a). The Meta-atoms of the Phased Array are made of PCMs. A Two-dimensional Row-electrical Signaling Architecture in a Row-column form is Designed to Change the Crystalline State of the PCM. (b) The Architecture in (a) is used for Interaction with Trapped Atoms or Ions for Quantum Applications

2.5.3 Generalized Spatial Light Modulators and Manipulators for Imaging/Spectroscopy/Computing

The ability to change the index of refraction of a PCM by a large amount at subwavelength scales enables the formation of reconfigurable MSs (e.g., Figure 27(a)) for spatial-spectral coding of an optical wavefront, i.e., to manipulate the amplitude, phase, polarization, and spectral content of an optical beam with subwavelength resolution. Such a powerful platform can be considered as a universal spatial/spectral light modulator (SLM, see Figure 27(a)) with unprecedented performance measures, including ultra-small unit cells (or pixels), fast reconfiguration (100's ns corresponding to a few MHz), low power consumption, large-scale (limited only by fabrication), and high dynamic range. The speed provided by the PCMs is excellent for several applications in imaging, spectroscopy, and computing. A unique feature of the proposed platform is its ultra-thin nature, which allows the integration of several MS layers to form a 2.5-dimensional (2.5D) reconfigurable architecture as the universal imaging/spectroscopy/computing cube (see Figure 27(c)). The actual functionality of such a cube can be programmed using the reconfigurable MSs. Note that not all the MSs in this 2.D platform need to be reconfigurable; having only a subset of them reconfigurable is sufficient to provide the needed degrees of freedom. The proposed platform would be very powerful not only as a single reconfigurable SLM, but also as a universal system for complete measurement of an optical wave (spatial, spectral, and polarization information). This goes far beyond conventional imaging systems where MSs are used as metalenses.

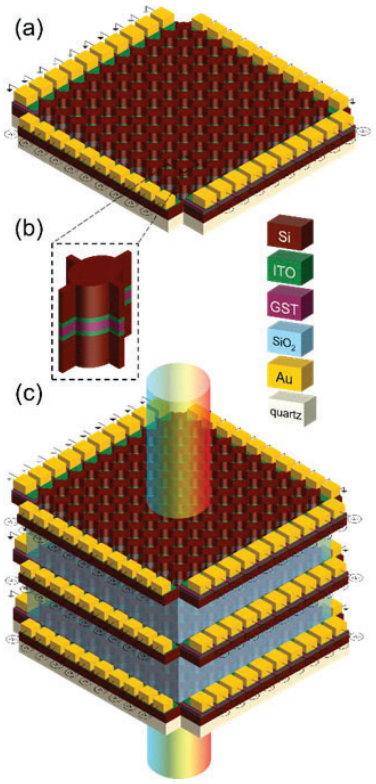

Figure 27: Representation of the Proposed 2D MS Consisting of an Array of Unit Cells (a), Schematic of a Unit Cell of the MS Structure Formed by Integration of Si and GST (b), Representation of the Proposed 2.5D (c) Reconfigurable Meta-cube Formed by Cascading the MSs in (a)

While the application of the 2.5D structure in Figure 27(c) for imaging and spectroscopy is evident, the use of this platform for enabling brain-inspired computing (e.g., implementing a neural-network (NN)-type architecture) should not be discounted. The reconfigurable multi-MS architecture perfectly mimics a multi-neuron platform in which each neuron can be modeled by a MS unit cell (which can incorporate several meta-atoms). The reconfiguration enabled by PCMs allows for controlling the interactions between neurons in adjacent layers to the level that light propagation allows such neurons to interact. One major advantage of the MS-based platform is the width of the NN it provides. Here, the width corresponds to the amount of data that can be placed in the network in parallel (i.e., the number of pixels in the first MS layer). This is the main advantage of optics over electronics even though electronics can provide a better depth (or many network layers). By implementing the NN-like architecture using the structure depicted in Figure 27(c) for the first few layers of a computing platform to condense the huge input data and moving the deeper layers to electronics, a novel hybrid photonic/electronic computing platform with far better capabilities than conventional electronic deep-learning architectures could be created. The effect of fabrication imperfections and environmental changes in the multi-MS architecture can be mitigated by focusing on specialized computing paradigms like a large array of weak-learners (WLs) as shown in Figure 28. Here, each WL is trained using a subset of the pixels in the final NN-type architecture to perform specific computing tasks (e.g., classification, recognition, clustering, etc.) with a reasonably small accuracy (e.g., 55-60%). Thanks to the huge parallelism of optics, many such independent WLs can be trained using the architecture in Figure 28 to collectively result in close to 100% accuracy. This architecture can be scaled to perform multiple tasks simultaneously. The number of tasks can be increased by reconfiguring the architecture using the reconfigurable MSs at multi-MHz speeds. This will be a truly practical path to brain-inspired optical computing with superior performance over electronics.

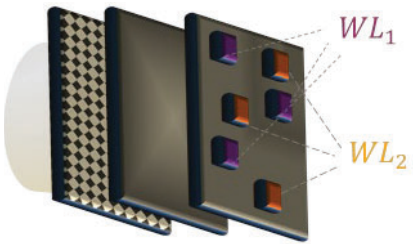

Figure 28: WLs in a Multi-MS Structure with Reconfigurable, Linear, and Nonlinear Layers

2.5.4 A Rich PCM Portfolio for Nanophotonics in the Visible-IR Wavelength Range

Having a set of reliable PCMs with low loss and a large refractive index change in different phases is essential for enabling the above applications. As such, we believe a thorough investigation of the possible materials for different wavelength ranges is a highly important research topic. The phase diagram shown in Figure 29 helps classifying promising chalcogenide-based PCMs. GeTe (the first discovered chalcogenide-based PCM) shows a relatively fast crystallization with a large optical contrast. Several other alloys such as $Ge_1Sb_4Te_7$, $Ge_2Sb_2Te_5$, and $Ge_1Sb_2Te_4$ have also been identified, all along a pseudo-binary line that connects the GeTe and Sb_2Te_3 compounds. Moving from GeTe towards Sb_2Te_3 on the pseudo-binary line, crystallization speed increases, glass temperature (T_g) and melting

temperature (T_m) decreases, and data retention (i.e., the retention of the amorphous state) decreases. In other words, Sb_2Te_3 offers the fastest crystallization speed. In contrast, GeTe offers the most stable amorphous phase. Therefore, a compromise between the crystallization speed and the amorphous stability can be made by selecting a ternary composition close to the center of the pseudo-binary line. For example, $Ge_2Sb_2Te_5$ offers a fast crystallization speed (< 20 ns) with a moderate T_g (100-150 ºC) that ensures a long-term data retention (~ 10 years). It is also important to note that deviation from the canonical stoichiometry (i.e., $(GeTe)_n(Sb_2Te_3)_m$; n, m: integers) reduces the switching speed, primarily because the crystallization proceeds through a slow phase-segregation step.

The switching behavior and the optical contrast, induced by the phase switching, can also be customized by changing the composition of a chalcogenide PCM, primarily through the substitutional doping of isoelectronic elements in ternary GST alloys. For example, the doping of GST alloys with selenium (Se) atoms forms a quaternary Ge-Sb-Se-Te PCM that is referred to as GSST. Recent studies show that an optimized addition of Se to the $Ge_2Sb_2Te_5$ alloy can significantly reduce the optical loss in the near-IR to the mid-IR spectral range. Indeed, the optimized GSST alloy (i.e., $Ge_2Sb_2Se_4Te_1$) shows a broadband transparency in the 1–18.5 μm wavelength range, while offering a large refractive-index change ($\Delta n \approx 2$) without a loss penalty (i.e., $\Delta k \approx 0$). Density-functional-theory (DFT) calculations show that increasing the Se content widens the bandgap of the GSST alloy, leading to smaller optical loss in the IR regime.

In Figure 29(a), we have presented some promising chalcogenide-based PCMs for operation in visible and near-IR regimes. Ideally, a PCM with a large Δn and a small Δk is desired. As described by the Kramers–Kronig relation, however, the real and imaginary parts of the refractive index are not independently controllable. Thus, the relative ratio of the index change to the loss change (i.e., $\Delta n/\Delta k$) serves as a figure of merit (FOM) for comparing various PCMs. As shown in the spider charts in Figures 29(b,c), for operation in visible and telecommunication wavelengths, Sb_2S_3 and $Ge_2Sb_2Se_4Te_1$ provide the best FOMs, respectively. For intermediate spectral range (i.e., near-IR), GeTe provides an optimal FOM. We note that such a conclusion is solely made based on the FOM. However, based on the switching speed, for instance, $Ge_2Sb_2Te_5$ offers a faster response than both $Ge_2Sb_2Se_4Te_1$ and GeTe. Therefore, in the selection of PCM materials, the ultimate application should be considered.

Finally, we would like to mention that, a more fundamental approach towards the identification of alternative PCMs can be pursued via considering the atomistic nature of the PCMs. Re-evaluating the portfolio of successful PCMs shows common characteristics that can be further employed for the identification and, yet better, prediction of alternative PCMs. First, all identified PCMs show distorted octahedral structures. Second, a relatively large density of intrinsic vacancies seems to be mandatory for the structural stability. Third, unlike most semiconductors with sp^3-hybridized bonds (i.e., a tetrahedral coordination), the atomic bonds in PCMs display p-type characteristics. The p-type bonding (i) guarantees the 6-fold coordination in the crystalline state, (ii) is prone to distortion (because it is weaker than sp^3 bonds), which is necessary for the crystal stabilization, and (iii) can be easily broken for the fast switching of bonds from octahedral to tetrahedral on amorphization. Interestingly, p-type bonding has been shown to occur in alloys with more than 4 valance electrons. Thus, considering these similarities, the search for new PCMs can be narrowed down to the alloys of group 15 and 16

elements with octahedral structures, more than 4 valance electrons, and proper T_g and T_m values. Also, special attention should be paid to the specific stoichiometry of PCM alloys to eliminate the phase segregation during phase-transition cycles, if the fast switching speeds is desired.

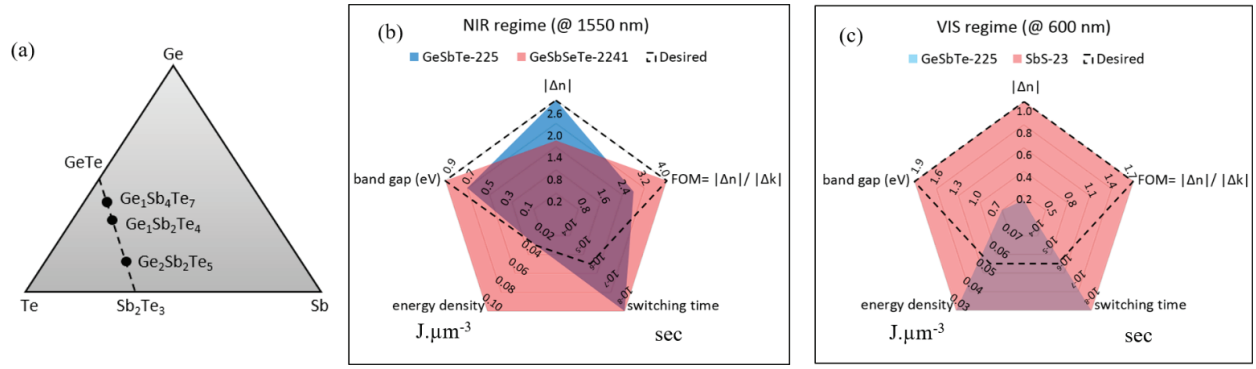

Figure 29: Alternative PCMs for Customized Applications

The phase diagram of the Ge-Sb-Te system (a). The dashed line shows the pseudo-binary line, which connects GeTe and Sb_2Te_3 compositions. Most popular GST-based PCMs can be identified on this line. (b, c) Spider charts of best known PCMs for operation in near-IR and visible regimes, respectively. FOM: figure of merit

In summary, considering the unique opportunities PCMs can bring into nanophotonics, especially for integrated photonic devices and systems over a large wavelength range, a thorough research for creating a rich portfolio of PCMs with a wide range of performance measures (e.g., FOM, speed, power consumption) for a wide range of operation wavelengths (from ultra violet (UV) to IR) can be very rewarding in enabling new applications while addressing several challenges caused by lack of sensitive active materials.

2.6 Conclusions: A New Platform for Ultra-miniaturization of Reconfigurable Integrated Photonic Systems

In summary, in this two-year seedling project we successfully demonstrated the unique features of the PCMs for enabling a new paradigm in design and implementation of reconfigurable integrated nano-photonic structures with unprecedented features. Although the overarching goal of this project was the demonstration of the ultra-miniaturized phase shifters for the MOABB program, our research has applicability well beyond the phase shifters originally focused on and enables the creation of a new platform that can be used to manipulate light strongly using subwavelength features. We strongly believe that the demonstrated hybrid Si (SiN)/PCM platform can address multiple challenges in the use of integrated photonics for state-of-the-art applications. It can enable a universal material platform for operation in the UV-IR range by proper integration of CMOS-compatible substrate with optimal PCMs for operation at desired wavelengths. We hope that this small-scale research motivates a larger and more sizable project in investigation of hybrid PCM-based materials and devices for integrated nano-photonics along the potential lines described in Section 2.5.

3 PUBLICATIONS AND PRESENTATIONS

3.1 Journal Papers

[1] H. Taghinejad, S. Abdollahramezani, A. A. Eftekhar, T. Fan, A. H. Hosseinnia, O. Hemmatyar, A. E. Dorche, A. Gallmon, and A. Adibi, "ITO-Based μ-Heaters for Multi-Stage Switching of Phase-Change Materials: Towards Beyond-Binary Reconfigurable Integrated Photonics," arXiv preprint arXiv:2003.04097 (2020).

[2] S. Abdollahramezani, O. Hemmatyar, H. Taghinejad, A. A. Eftekhar, A. H. Hosseinnia, T. Fan, and A. Adibi, "An Optically-controlled Hybrid Platform for Reconfigurable Integrated Nanophotonics using Phase-change Materials," under preparation for submission to Advanced Photonics in July 2020.

[3] S. Abdollahramezani, H. Taghinejad, A. A. Eftekhar, A. H. Hosseinnia, T. Fan, O. Hemmatyar, and A. Adibi, "Hybrid Platform for Miniaturized Reconfigurable Integrated Photonic Devices using Thermally-controlled Phase-change Materials," under preparation for submission to Optics Letters in July 2020.

[4] A. A. Eftekhar, S. Abdollahramezani, H. Taghinejad, O. Hemmatyar, A. H. Hosseinnia, T. Fan, and A. Adibi, "Reconfigurable Integrated Photonic Switches enabled by Optically controlled Phase-change Materials," under preparation for submission to Optics Letters in July 2020.

3.2 Refereed Conference Papers

[1] S. Abdollahramezani, H. Taghinejad, T. Fan, A. A. Eftekhar, O. Hemmatyar, A. H. Hosseinnia, A. E. Dorche, and A. Adibi, "Reconfigurable Si/SiN-based integrated photonic devices enabled by integration with phase change materials," in SPIE Photonics West Proceedings, San Francisco, CA, 2020.

[2] S. Abdollahramezani, H. Taghinejad, T. Fan, A. A. Eftekhar, A. H. Hosseinnia, and A. Adibi, "Integrated Nanophotonic Structures for Enhanced Light-matter Interaction," **Invited** talk in SPIE Photonics West Proceedings, San Francisco, CA, 2020.

[3] A. Adibi, "Hybrid Material Platforms for Low-power, High-speed, and Miniaturized Integrated Nanophotonic Devices and Systems," Finisar, San Diego, CA, 2019. (**Invited** seminar talk)

[4] A. H. Hosseinnia, N. Sodagar, H. Moradinejad, T. Fan, A. A. Eftekhar, and A. Adibi, "Hybrid Material Platforms for Low-power, High-speed, and Miniaturized Integrated Photonic Devices and Systems," Optics and Photonics Conference, Philadelphia, PA, 2018. (**Invited keynote** talk).

[5] A. H. Hosseinnia, N. Sodagar, H. Moradinejad, T. Fan, A. A. Eftekhar, and A. Adibi, "Hybrid Material Platforms for Reconfigurable Integrated Nanophotonics," Stegeman Symposium. Orlando, FL, 2018. (**Invited** conference talk)

[6] A. H. Hosseinnia, N. Sodagar, H. Moradinejad, T. Fan, A. A. Eftekhar, and A. Adibi, "Hybrid Material Platforms for Low-power, High-speed, and Miniaturized Integrated Nanophotonic Devices and Systems" Samsung USA, San Jose, CA, 2018. (**Invited** seminar talk)

LIST OF ABBREVIATIONS, ACRONYMS, AND SYMBOLS

ACRONYM	DESCRIPTION
3D	Three Dimensional
AFM	Atomic-Force Microscopy
Ar	Argon
Au	Gold
CMOS	Complementary Metal–Oxide–Semiconductor
DARPA	Defense Advanced Research Projects Agency
dB	Decibel
DC	Direct Current
DFT	Density-Functional-Theory
DoD	Department of Defense
FDTD	Finite-Difference Time-Domain
FOM	Figure Of Merit
FSOC	Free-Space Optical Communications
GeTe	Germanium Telluride
GST	Germanium Antimony Telluride
GTRI	Georgia Institute of Technology
HfO_2	Hafnium Oxide Toxicity
IR	Infrared
ITO	Indium Tin Oxide
LiDAR	Light Detection and Ranging
LPCVD	Low-Pressure Chemical Vapor Deposition
MOABB	Modular Optical Aperture Building Blocks
MSs	Metasurfaces
mW	Milliwatt
MZI	Mach-Zehnder Interferometers
NN	Neural-Network
ns	Nanoseconds
PCM	Phase-Change Materials
pJ	PicoJoules
PMMA	Polymethyl Mathacrylate
RF	Radio Frequency
RIE	Reactive Ion Etching
RTA	Rapid Thermal Annealing
SCCM	Standard Cubic Centimeter per Minute
Se	Selenium
SEM	Scanning Electron Microscope
Si	Silicon

ACRONYM	DESCRIPTION
SiC	Silicon Carbide
SiN	Silicon Nitride
SiO_2	Silicon Dioxide
SLM	Spatial/Spectral Light Modulator
TBR	Thermal Boundary-Resistance
T_g	Glass Temperature
Ti	Titanium
T_m	Melting Temperature
UV	Ultra Violet
WLs	Weak-Learners
XPS	X-ray Photoelectron Spectroscopy